Synthesis, Characterisation, Post-synthesis Processing and Applications of Transition Metal Dichalcogenides: A focus on WSe_2

CHAN XINHUI KIM
A0074136J

In Partial Fulfilment of the Requirements for the Degree of Bachelor of Science with Honors

Department of Physics
National University of Singapore
2013/2014

Table of Contents

List of Figures

List of Graphs

List of Tables

Acknowledgments

The journey towards the submission of this final year project has been one full of tears and joy, falling and getting back up, and it has let me learn a lot about myself in many ways. There are many people I wish to thank without whom this project would have not been completed.

First, I would like to express my sincere thanks to my supervisor Associate Professor Sow Chorng Haur, for all his guidance throughout the project. He has been amazingly patient, ever-willing to help despite his very busy schedule and has truly enthused me with his passion for teaching and for nano materials. Words cannot describe how blessed I am to have him as my supervisor.

Next, my mentor, Lu Junpeng, for the time he takes off to patiently teach me how to use the various instruments and for explaining various concepts to me. His advice has been invaluable. I am also very grateful to Associate Professor Tok Eng Soon, who has helped me with his expertise and to Dr. Pan Jisheng for helping me with XPS.

I also want to thank my lab buddies: Minrui, Lili, Kim Yong, Hao Fatt and Sharon for helping me when I am lost and am not sure what my next step should be. Also, I want to thank my fellow FYP friends, Jiahui, Hongji and Yin Chi for caring so much for me and providing such great support. I will never forget the fun times we shared in our lab (and of course, our nanocat (ket)).

I want to thank my family, friends and loved ones (including my dog) for being my source of strength and comfort. Thank you for being so tolerant of my busy schedules, and for sharing my stressful moments with me.

Last but not the least, I want to thank God, without whom none of these would have been possible. He has really taught me to rely on His everlasting mercies and grace. To God be the glory, the best is yet to be.

Abstract

The monolayer transition metal dichalcogenides (TMDs) have attracted much attention of researchers due to their potential applications in electronic and optoelectronic devices. Among these TMDs, WSe_2 is demonstrated as one of the most promising two dimensional (2D) materials due to its layer-dependent physical and chemical properties that arise in its monolayer form, such as the indirect to direct band gap transition and photoluminescence transition. Here, we reported the growth of large-area uniform WSe_2 nanolayers using a chemical vapour deposition (CVD) method in a horizontal tube furnace. The CVD method used in our experiments utilises WO_3 and Se powder precursors with an Ar/H_2 gas, where the introduction of hydrogen helps to activate the selenisation of WO_3. We also reported the usage of focused beam laser irradiation as a post-synthesis technique. We found that this technique reduces the layer thickness of the WSe_2 flakes. It also causes WSe_2 to exhibit increased photo response, as seen in an increase in an order of magnitude of the dark and photocurrent after laser modification was conducted in ambient conditions. An investigation was done to determine the surface composition of the WSe_2 after laser modification in ambient and vacuum conditions. It was found that the ratio of W^{6+} ions in the WO_3 environment increases after laser modification in ambient conditions and decreases after laser modification in vacuum conditions as compared to the as-synthesised WSe_2 film. The introduction of defect states related to WO_x is suggested as a reason for the increased photocurrent after laser modification in ambient conditions.

Chapter 1

1 Introduction

The recent advent of research in graphene and the discovery of its many desirable properties have inspired research into other two-dimensional (2D) materials such as transition metal dichalcogenides (TMDs). The TMDs in their bulk forms have been studied for years, particularly in their usefulness as solid state lubricants[1], but it is the 2D form of TMDs that has attracted the attention of the scientific community in recent years. 2D Much research into the synthesis, characterization and application of 2D TMDs such as MoS_2, $MoSe_2$, WS_2 and WSe_2 has been carried out[2-12]. In particular, research into MoS_2 has garnered much success[2, 13, 14].

TMDs share similar layered structures, in which each layer comprises three atomic planes: a hexagonally arranged transition metal atoms sandwiched between two hexagonal lattices of chalcogen (S, Se) atoms. The interlayer atoms are bonded by strong covalent bonds while the adjacent layers are weakly bonded by van der Waals bonding.

The layer-dependent properties of TMDs have generated a great deal of attention. One attractive property is the transition from an indirect band gap to a direct band gap when TMDs are thinned down from bulk to monolayer. For example, monolayer MoS_2 is a direct gap semiconductor with a band gap of 1.90eV. This distinguishes it from its bulk counterpart with a smaller indirect band gap of 1.29eV. The sizable band gap in 2D TMDs paves the way for widespread applications in electronics such as field-effect transistors (FETs)[7, 14, 15] and optoelectronics such as phototransistors[16, 17].

Despite its wide array of attractive electronic properties such as a high carrier mobility[18], the application of graphene is intrinsically limited by its small band gap. This means that graphene-based FETs cannot be effectively switched off and cannot achieve

a high on/off ratios desirable in high-frequency applications, even though physical and chemical methods such as lithographic thinning of graphene nanoribbons and chemical functionalization have been discovered to tune its band gap[19, 20]. On the other hand, FETs fabricated with atomically thin layers of MoS_2 can achieve high channel mobility of up to 60 $cm^2V^{-1}s^{-1}$ [13, 21] at 250K and high on/off ratios in the order of 10^8, making MoS_2 superior in logic transistor applications[14]. The direct band gap results in photoluminescence, presenting great potential in application of TMDs in optoelectronics. When reduced to monolayer thickness, TMDs show large optical absorption greater than 10^7 m^{-1} across the visible range[22]. This makes them useful for photovoltaic devices. Photodetectors based on monolayer MoS_2 have been shown to exhibit photoresponsitivity of up to 880 A W^{-1} [17].

To tap into these exciting properties and turn the corresponding potential applications into a reality, an effective synthesis approach to achieve ultrathin 2D TMDs from their bulk counterparts is needed. Hence, the objectives of this thesis are the following: First, to further understand the growth mechanism of WSe_2 and optimize its growth conditions, CVD growth of WSe_2 will be explored. Using this growth method, we expect to synthesize monolayer WSe_2 film with reasonably large areas. Next, the characterisation of the synthesised WSe_2 will be done. In addition, post-synthesis laser modification of WSe_2 via a focused laser beam technique will be examined. The motivation for this is found in Section 2.3. Finally, a simple photodetector device is fabricated to investigate and compare the photocurrent properties of WSe_2 before and after laser modification.

Chapter 2

2 Background

2.1 Tungsten Diselenide

WSe_2, like the other TMDs, has a layered structure. It comprises 3 hexagonally packed layers, Selenium-Tungsten-Selenium, where the tungsten layer is sandwiched between the two hexagonally packed selenium atomic planes (Figure 2.1.1). One monolayer has a step height of ≈0.7nm[7, 10]. Within each layer, WSe_2 exhibits a trigonal prismatic atomic structure where the W-W bonds are 3.28Å long[1]. The atoms in each layer are bonded together by strong covalent bonds while the sandwich layers are coupled by weak Van der Waals forces. This allows for easy micromechanical cleavage into the separate 2D layers of WSe_2.

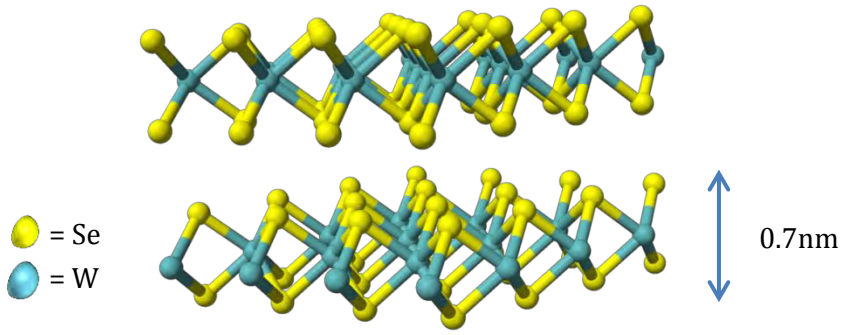

Figure 2.1.1: Layered Structure of WSe_2 monolayer (©Ben Mills, Wikipedia Commons)

WSe_2 is in the same family of TMDs as MoS_2.[1] Recently, it has been found that mechanically exfoliated WSe_2 atomic sheets also show similar high in-plane carrier mobilities as MoS_2 [7]. A unique property of WSe_2 is that it has been shown to show ambipolar characteristics, combining both p- and n- type behaviours in the same material, depending on the metal contact used[7, 10, 23]. If the high work function metal Pd is used, a p-type behaviour is shown and an n-type behaviour can be obtained by using

In as the contact metal[6]. Designing a multi-layer FET with Ni as the source and Pd as the drain electrode would be useful in electronic transistor applications.

WSe_2 has been identified as an important narrow band gap semiconductor. When in its bulk form, it has an indirect band gap in the near-infrared frequency range (~1.21eV) [12] characterized by the jump between valence band maximum at the Γ point and the conduction band minimum in middle of the Γ-K band. However, when thinned down to a 2D monolayer, the band gap transits into a direct band gap (~1.64eV) in the visible region of the electromagnetic spectra [11] characterized by the jump in the K point of the Brillouin zone[5]. This is due to the quantum confinement effect[24]. The direct band gap of monolayer WSe_2 allows for more effective electron-hole pair generation under photoexcitation, leading to enhanced photoluminescence. This makes monolayer WSe_2 attractive for optoelectronic device applications. Based on these properties, we will demonstrate the optoelectronic application of monolayer WSe_2 film as high performance photodetectors in this thesis.

2.2 Chemical Vapour Deposition

Chemical Vapour Deposition (CVD) is a technique of thin film growth in which the source material is vapourised at high temperatures, and condenses on a substrate at a lower temperature region. CVD is often conducted in a tube furnace. There are a few processes involved in CVD, namely: 1) vaporisation of source materials, 2) transport of source materials (in the direction of flow of carrier gas) towards the substrate 3) adsorption on the substrate surface 4) nucleation on substrate surface followed by surface processes such as diffusion and reaction of adsorbed species with each other 5) desorption of adsorbed species into main gas stream[25]. This is more clearly seen in Figure 2.2.1.

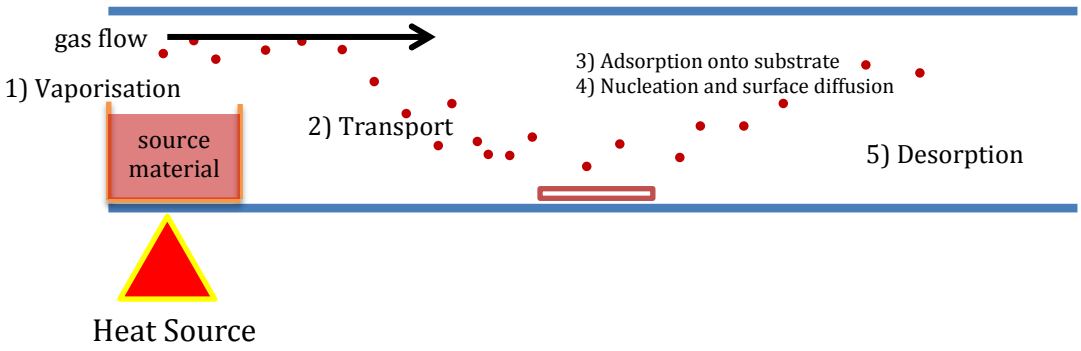

Figure 2.2.1: CVD processes in a tube furnace

There have two main approaches to the synthesis of 2D TMDs: top-down and bottom-up methods.

Top-down methods generally involve exfoliation of TMD flakes from their bulk. One common method is micromechanical cleavage with adhesive tape which has been shown to create high-quality crystalline flakes[9]. Mechanical exfoliation is made possible by the weak van der Waals bonding between layers in the layered structure of TMDs. However, mechanical exfoliation is a random process which has low yield. The drawback of this method is the lack of control of flake thickness and size needed for device applications[3]. Other exfoliation methods include liquid exfoliation by direct sonication which is able to produce large quantities of TMD film, but is unable to control the layer thickness to a single layer nanosheet[3].

Bottom-up methods such as chemical vapour deposition (CVD) growth of 2D TMDs have also been explored, where solid precursors heated to high temperatures are vapourised and co-deposited on nearby substrates[8, 26]. CVD growth has been shown to produce high quality and large area TMD films[8, 26, 27]. There are many methods for CVD formation of TMD films, such as the direct sulphurisation or selenisation of the transition metal film[28] and the vaporisation of metal oxide and chalcogen powders followed by their deposition on substrates[26]. The growth of the 2D TMDs is largely influenced by the concentration and/or amount of precursors used, as well as the

temperature and the pressure conditions in the furnace. This will be explored in Section 4.1.

2.3 Focused laser beam modification

Monolayer WSe_2 is highly sought after for its unique optoelectronic properties[2, 5, 23, 29]. However, it is often difficult to produce a monolayer film through top-down and bottom-up synthesis methods due to the poor control of layer thickness. Even in the CVD process used in this experiment, it is found that slight variations of pressure in the furnace during the growth process lead to different WSe_2 layer thickness. It is difficult to achieve a uniform nucleation of WSe_2 on the substrate. Further, CVD growth may lead to impurities formed on the grown films. There has been research done on post-synthesis methods to generate single-layer MoS_2 on demand. Some methods found include thermal annealing[30], Ar^+ plasma[31], and laser thinning[32]. The advantage of laser thinning is its easy accessibility as well as its potential in fabricating "on-demand" single layers of MoS_2. The suggested mechanism of thinning MoS_2 by using laser is as follows: the upper layers are sublimed due to the heat induced by light absorption from the laser. Due to the weak van der Waals forces between layers, heat cannot easily dissipate through the substrate. The bottom layer remains on the substrate unless much higher laser powers are used because it is in intimate contact with SiO_2/Si substrate (heat sink). An incident laser power density lower than $80mW/\mu m^2$ does not seem to affect the MoS_2 layers while power densities between $80 - 140mW/\mu m^2$ appear to thin the MoS_2 flakes down to a single layer[32].

The laser thinning of WSe_2 based on a similar idea as in the laser thinning of MoS_2 would be a feasible strategy. To our knowledge, the post-synthesis thinning of WSe_2 flakes of varying thicknesses has not been reported. In this thesis, we will investigate how laser modification of WSe_2 in both ambient conditions and in vacuum

conditions affects its morphology and number of layers, and subsequently investigate if laser modification has any effect on its optical, electrical and photoelectrical properties.

Chapter 3

3 Experimental Methodology

3.1 Synthesis of WSe_2 on sapphire

The aim of the synthesis is to achieve high-quality large-area uniform layers of WSe_2 for characterization in nanomaterials research. CVD has been reported to produce large-area and highly crystalline WSe_2 nanosheets[8] and is used in our experiment.

The synthesis is carried out in a 2.54 cm diameter single zone horizontal tube furnace via the CVD process. One end of the tube is connected to a mechanical pump and the other to a mass flow controller with gas sources. Figure 3.1.1 shows a schematic diagram of the tube furnace. Photographs of the furnace and the set-up are attached in Figure 3.1.2.

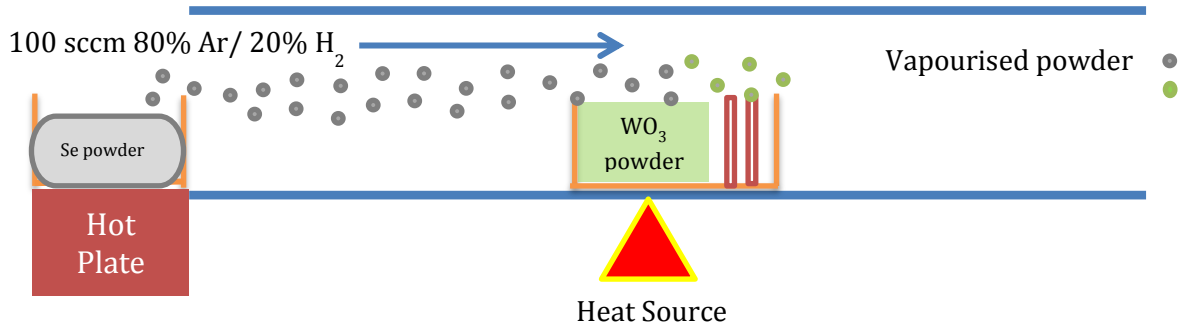

Figure 3.1.1 Schematic diagram of tube furnace

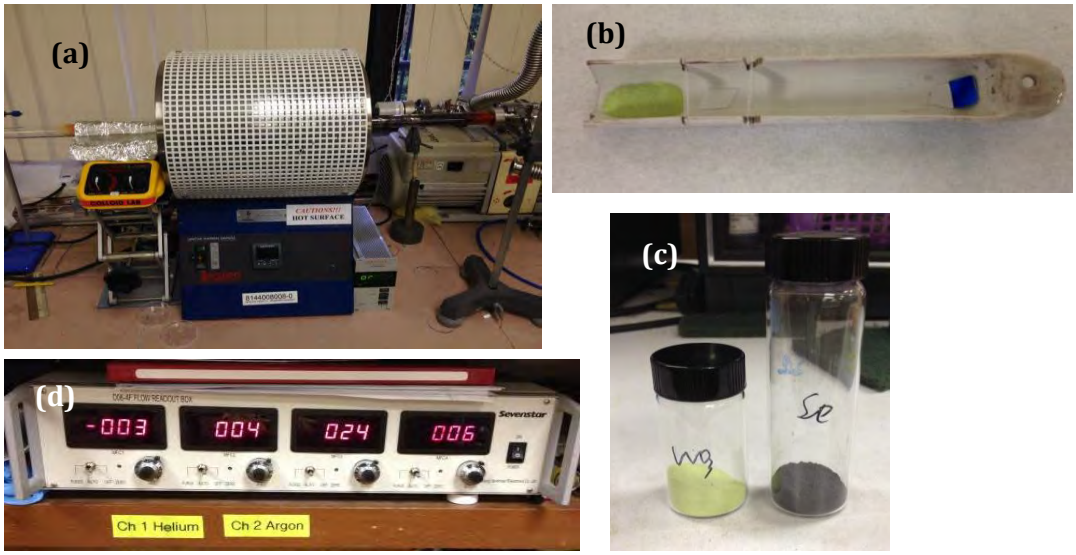

Figure 3.1.2: Photographs of tube furnace set-up (a) Tube furnace (b) ceramic boat with sapphire substrate and WO_3 powder (placed near middle of furnace) (c) WO_3 and Se powder precursors (d) Mass flow controller

The precursors used are powdered forms of Se and WO_3. The Se powder is placed upstream in a ceramic boat which is outside the furnace, where the temperature can be controlled by a hot plate. The WO_3 powder is placed a separate ceramic boat near the centre of the furnace. The substrate, c-sapphire (001), is placed in the same boat as the WO_3 powder, with varying distances from the centre of the furnace. Before the temperature is raised, the pressure in the furnace is pumped down to a pressure of $3x10^{-3}$ Torr using the mechanical pump. Under a continuous 100 sccm flow of a gas containing 80% Ar/20% H_2, the furnace temperature is raised at a ramping rate of 28°C/min and the pressure was maintained at 3.6 Torr. When the temperature within the furnace reaches 800°C, the hot plate is switched on and maintained at 290°C. The highest temperature the furnace reaches is 950°C, and this temperature is held for 15 minutes for growth to occur. After the heating process, the furnace is naturally cooled down to room temperature.

3.2 Focused laser beam technique

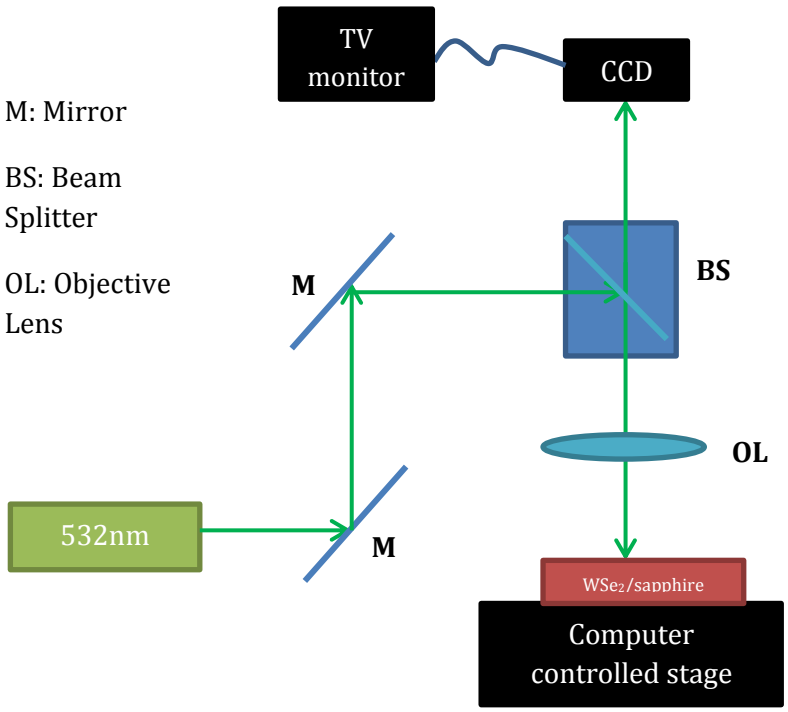

Figure 3.2.1: Schematic diagram of laser cutting system

Figure 3.2.1 shows a schematic diagram of the system used for laser modification. The sample is placed onto a computer-controlled stage and a computer programme is set to control the movement of the stage. The laser beam (λ = 532nm) is focused on the sample with the focused laser spot diameter ~1μm. To study the effects of laser modification on WSe_2 (Section 4.3), an incident laser power of 173mW (power density = 220mW/μm^2) is used to make a quick cut through a WSe_2 triangle until a visible optical contrast can be observed on the TV monitor. For photocurrent comparisons (Section 4.4), a raster scan of a 50 × 100 μm^2 region with a laser power density 220mW/μm^2 is done between the two electrodes, particularly ensuring that the WSe_2 triangles between the electrodes have been laser modified. The laser modification for photocurrent comparisons are done in ambient conditions.

3.3 Characterisation of laser modified WSe_2 using SEM, AFM, XPS and Raman Spectroscopy

In this thesis, field emission scanning electron microscopy (SEM JEOL, JSM-6700F), atomic force microscope (AFM, Dimension Instruments 3000), Raman Mapping (Witec LD-WL206, 532nm), Raman spectroscopy (Reinshaw Invia Raman microscope, 532nm) and X-ray Photoelectron Spectroscopy (XPS, ThetaProbe) using a monochromatic Al Kα source (1486.7eV, spot size = 400μm) were used for characterization.

SEM was used to check the morphology of the WSe_2 triangular flakes on the sapphire substrate. Nanostructure thickness was analyzed using tapping-mode AFM. Raman mapping and Raman spectroscopy were used to test for the presence of WSe_2 and to check for any changes in crystalline quality before and after laser cutting. XPS was used to characterize the surface composition of as-grown and the laser modified WSe_2 under ambient and vacuum conditions.

3.4 Fabrication of photodetector device on WSe_2/sapphire

The device fabrication was facilitated by the standard Electron Beam Lithography (EBL) technique. Ti/Au electrodes with the thickness of 5/30 nm were deposited via thermal evaporation. After that, the device is wire-bonded and loaded into the measurement set-up. The electrodes are positioned such that at least 1 WSe_2 triangles fall between the electrodes. The gap between the 2 Au electrodes is 5 μm. A schematic diagram of this is seen in Figure 3.4.1.

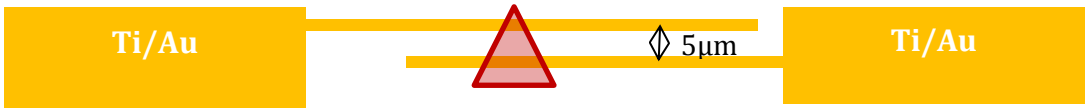

Figure 3.4.1: Schematic Diagram of Device: Ti/Au electrodes on WSe_2/sapphire

3.5 I-V and Photocurrent measurement

Figure 3.5.1: Schematic diagram of electrical connections of device

Figure 3.5.1 shows the electrical connections of the device, which is electrically connected to a sourcemeter (Keithley 6430 Sub-FemtoAmp Remote). The sourcemeter is able to provide a sweeping DC bias voltage and can measure current. The characterization of the device was carried out under ambient conditions at room temperature.

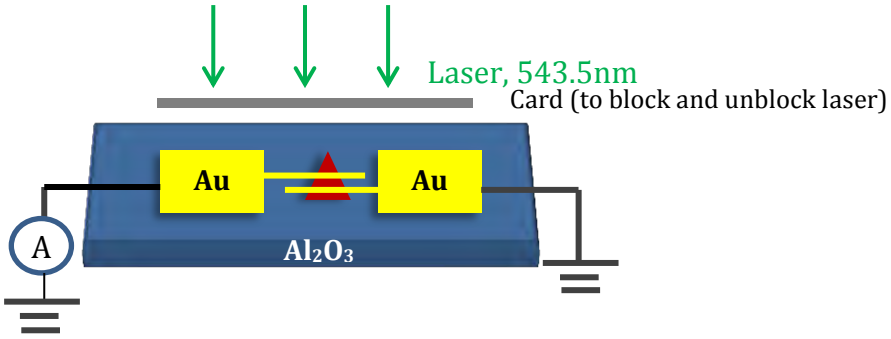

Figure 3.5.2: Schematic Diagram of Photocurrent Detection and Measurement System

A continuous wave laser beam λ = 543.5nm with power = 3.63mW was used to globally irradiate the device. In global irradiation, the laser source is mounted on top of the device so that the electrodes and their contact with the WSe_2 flake are uniformly illuminated (Figure 3.5.2). Dark I-V curves and I-V curves under global laser irradiation are obtained. These measurements were done under a sweeping voltage of -5V to +5V.

The photo response characteristics were determined by measuring current passing through the electrodes as a function of time while the laser beam is turned "on" and "off". The "on" state refers to the global irradiation of the laser beam on the device and the "off" state refers to using a card to block the laser beam from the device which achieves a dark condition.

The I-V and photoresponse characteristics are obtained after laser modification of the sample. Laser modification is done by rastering a 50 × 100 μm^2 region with a laser power density 220mW/μm^2 on the area between the two electrodes (Figure 3.5.3), ensuring that the WSe_2 triangles between the electrodes have been laser modified. The laser modification for photocurrent comparisons are done in ambient conditions.

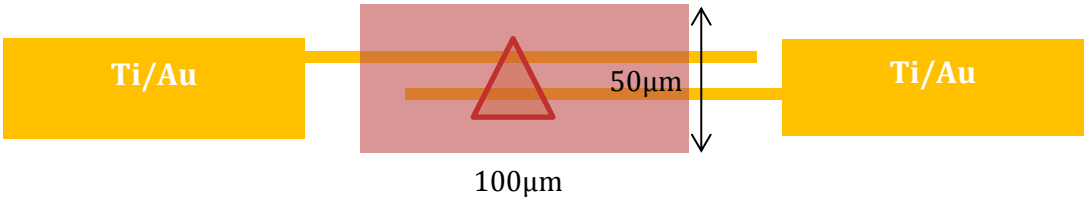

Figure 3.5.3: Schematic diagram of Device and laser cut region

Chapter 4

4 Experimental Results and Discussion

4.1 Synthesis

The morphology of the WSe_2 flakes and their lateral dimensions vary with the substrate temperature, which is controlled by placing the substrates at various distances from the source of heating. The temperature profile of the tube furnace shown in Figure 4.1.1 is only approximate as it cannot be measured in-situ under experimental conditions. The temperatures are measured using a thermocouple with furnace temperature kept at 950°C.

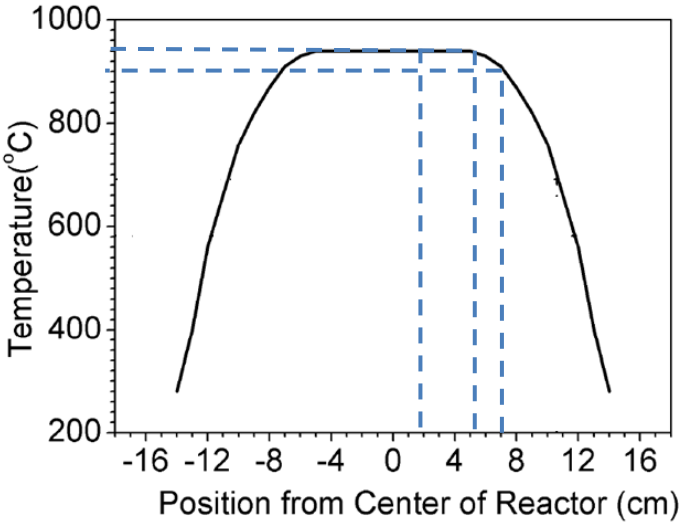

Figure 4.1.1: Temperature profile of tube furnace with varying distances from the centre

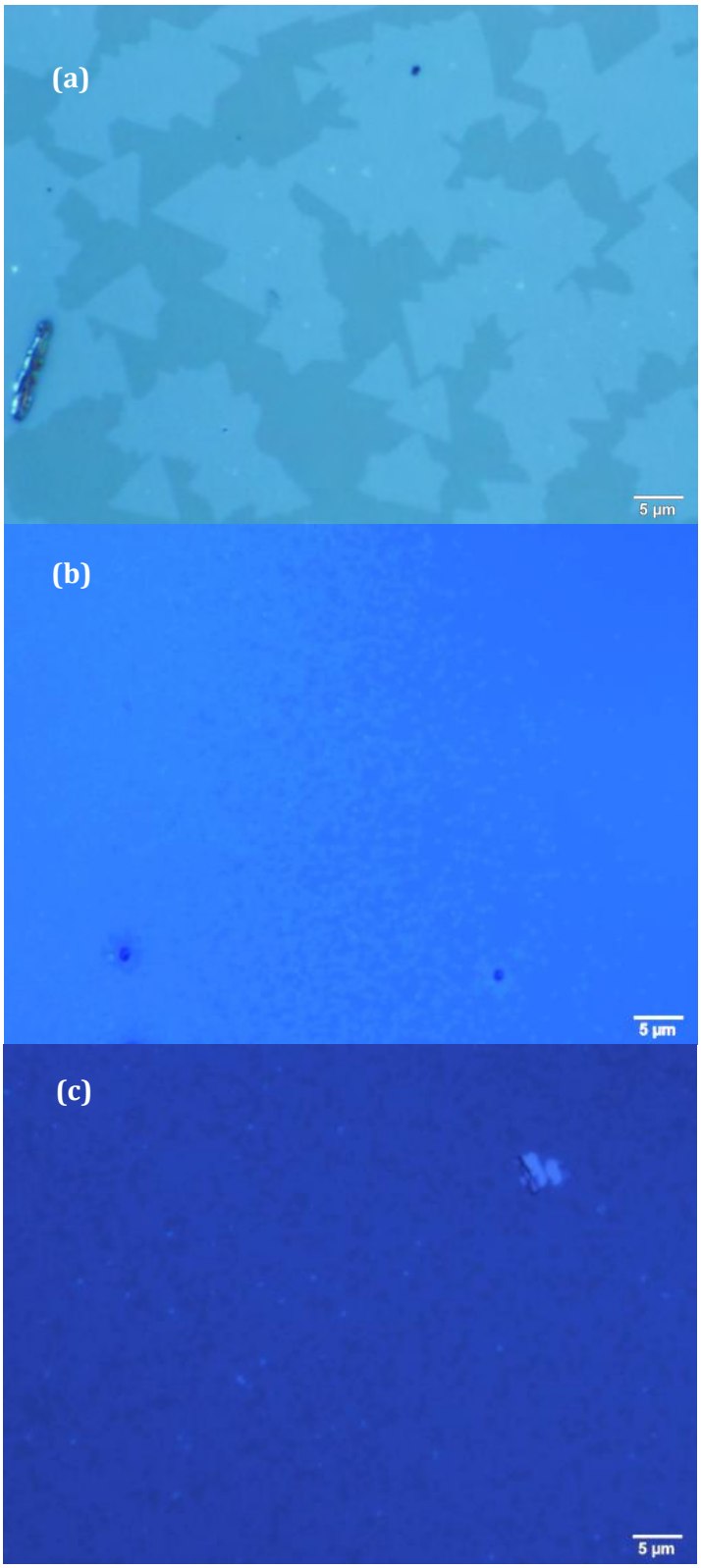

Figure 4.1.2: Optical images of WSe_2 morphology on sapphire substrate with varying distances from heat source (a) 2-3 cm (b) 4-5 cm (c) 6-7cm

Figure 4.1.2(a) shows the optical image of the products grown at a location about 2 - 3cm away from the heat source. The substrate temperature is approximately 950°C. The WSe_2 triangles are about 10 - 30μm in size, with the lateral dimensions limited by the lattice mismatch between WSe_2 and sapphire substrate. They are sparsely nucleated.

Further away at 4-5 cm from the heat source, the triangles are more densely nucleated and they start to form a continuous film. This is seen in Figure 4.1.2(b) (contrast adjusted for clearer resolution of details). At about 6 - 7 cm away from the heat source, the temperature is approximately 900°C. The triangles get even more densely nucleated (Figure 4.1.2(c)). This is expected as a lower temperature tends to favour higher nucleation densities in thin film growth.

The chemical equation that ensues in the CVD process is as follows:

$$WO_3\,(s) + 3Se\,(s) + H_2\,(g) \rightarrow WSe_2\,(s) + H_2O\,(g) + SeO_2\,(g)$$

Following a previous report by Lee et al.[26], the presence of H_2 is not required in the synthesis of MoS_2. However, H_2 plays the role of a reducer in this equation and is required in our growth approach of the formation of WSe_2 since Se is less reactive compared to S [8].

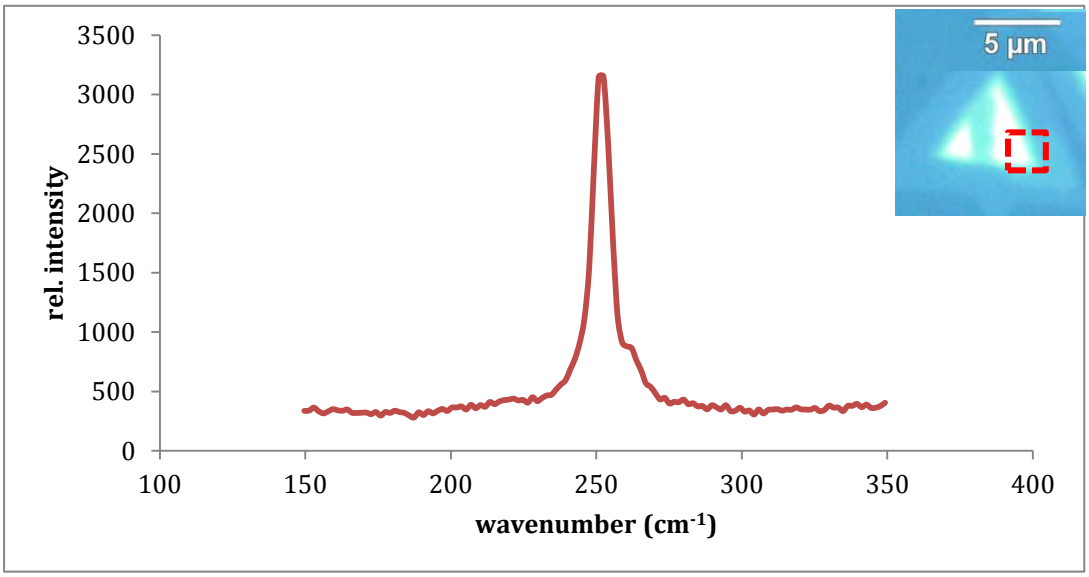

Graph 4.1.1: Raman Spectrum of as-grown WSe_2 flake (Inset: region where spectrum is taken)

To investigate the lattice structural property of the products, Raman spectroscopy was carried out and shown in Graph 4.1.1. WSe_2 has two Raman active modes: the main peak corresponding to the in-plane E_{2g} mode (≈ 250cm^{-1}) and the out-of-plane A_{1g} mode about 11cm^{-1} to the right of the main peak[11]. The Raman spectra obtained from the synthesized WSe_2 triangles in this work shows a strong E_{2g} peak at ≈ 251cm^{-1}, and a weaker A_{1g} peak at ≈ 261cm^{-1}. This confirms the presence of WSe_2 produced in our CVD process. The inset in Graph 4.1.1 shows the region where the Raman spectrum was obtained.

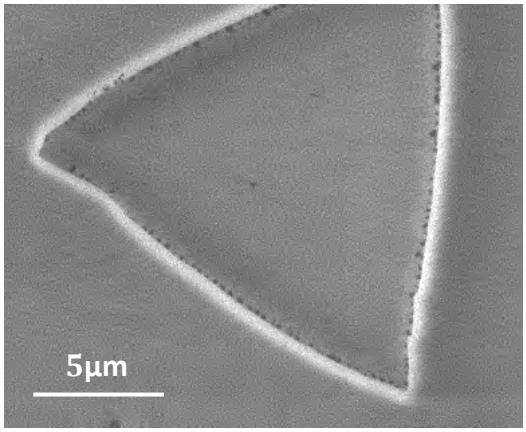

Figure 4.1.3: SEM image showing particles at edges of a WSe_2 flake

Based on SEM images of a single WSe_2 triangle (Figure 4.1.3), it can be observed that there are many particles forming around the edges of the triangles, while close to none are found on the top surfaces of the triangles. In light of this, a growth mechanism largely attributed to the chemical anisotropy of WSe_2 can be suggested. This was previously reported by Xu et al[12]. First, the source powder sublimes into gaseous molecules and the source vapour is transported to sapphire substrate. When it reaches the substrate, the vapour sublimes and the particles nucleate stochastically. As the substrate is heated to a high temperature, surface diffusion occurs. The particles diffuse to the edges of the nucleation nuclei, and the crystal grows along the lateral dimension. This is largely because the dangling bonds of the boundary atoms are more reactive and

thus absorb more particles. The top surface is passivized with chemically saturated Se atoms; hence the growth proceeds laterally across the surface into a film rather than vertically into 3D islands[12]. However, the identity of the particles is unknown.

As Se is used in excess to fully convert WO_3 to WSe_2 during the growth process, the products could be easily contaminated by the excessive Se powder. This is observed in Figure 4.1.4 and in the Raman spectrum seen in Graph 4.1.2. The Raman spectrum shows the Se peak corresponding to ~240cm^{-1} and a weaker peak at 251cm^{-1} which corresponds to WSe_2.

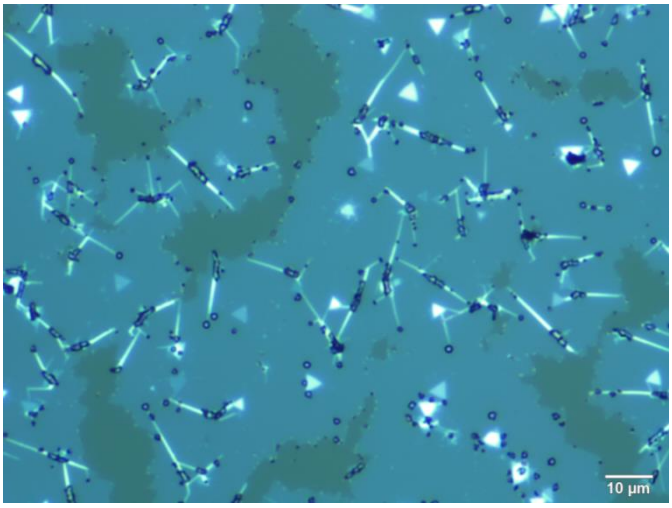

Figure 4.1.4: Dirty sample of WSe_2 (3.7 Torr)

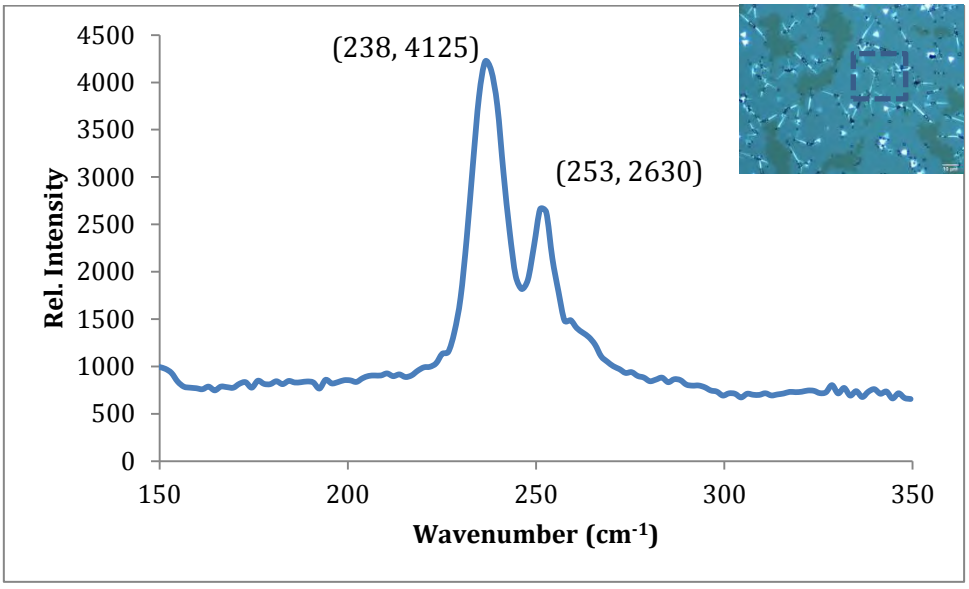

Graph 4.1.2: Raman spectrum of dirty WSe_2 flake with Se peak (Inset: region where spectrum is taken)

4.2 Laser Scanning

It has been found that MoS_2 flakes do not get affected by incident laser powers below 10mW (80mW/μm^2) but get thinned down to a single layer with powers between 10-17mW (80–140mW/μm^2). Similar to MoS_2, WSe_2 does not present any visible morphological change or optical contrast when cut with an incident laser power below 100mW (corresponding to a power density of < 127mW/μm^2) and velocity of laser = 20μm/s. The similar observations suggest that a similar mechanism as MoS_2 (refer to Section 2.3) may be assumed in a WSe_2 system as well.

4.3 Characterisation of WSe_2 (before and after laser scanning)

In this section, the laser beam technique will be studied for two of its functions:

(1) as a way to remove Se contamination on substrate surface, and

(2) as a means of thinning down WSe_2 flakes and modifying its physical properties.

The characterisation techniques presented below are conducted both before and after laser scanning so that comparisons may be made.

4.3.1 Optical Images

In order to remove the aforementioned Se contamination on the substrate surface, an effective post-synthesis cleaning approach is desirable. In this thesis, our developed focused laser beam technique has been employed to achieve the post-synthesis laser cleaning. Using laser of varying power densities, it is observed in both optical images (Figure 4.3.1) and Raman spectra (Graph 4.3.1) that Se may be completely removed from the surface of the substrate. However, the power density (64mW/μm^2) is too low to destroy the WSe_2 that has been synthesised, hence only the Se contamination is removed. Graph 4.3.1(a) shows a strong Raman peak at Se 238 cm^{-1} and a weaker peak at 253cm^{-1} which corresponds to WSe_2. The Se peak disappears upon laser scanning and the E_{2g} and A_{1g} WSe_2 peaks at 251cm^{-1} and 263cm^{-1} become stronger.

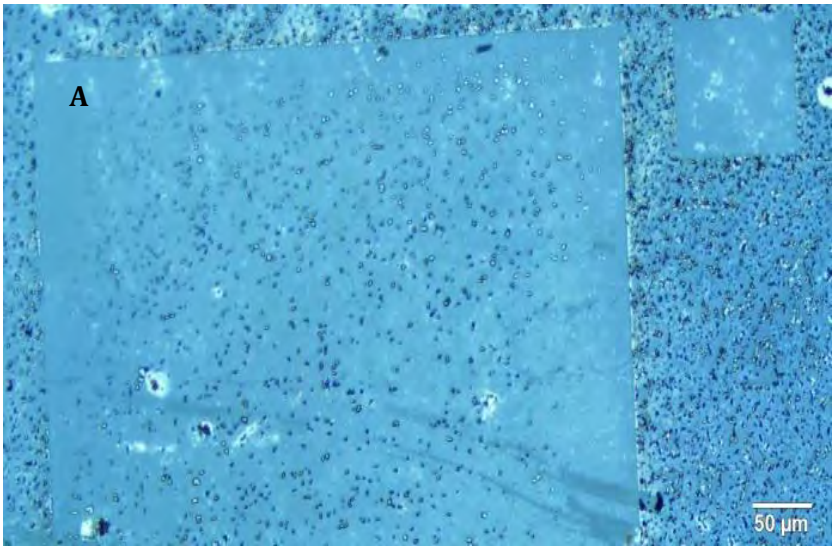

Figure 4.3.1: Laser cutting as a means to remove excess Se from surface.
The square on the left was cut with 64mW/µm², 50µm/s, and on the right with 64mW/µm², 20µm/s,

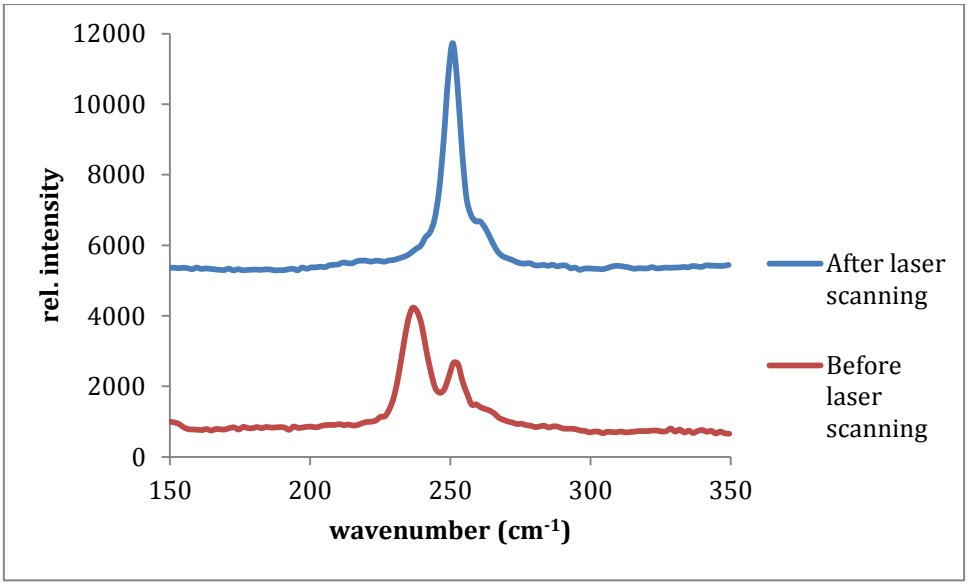

Graph 4.3.1: Raman spectra of dirty WSe_2 flake (a) Before (b) After laser scanning

Besides laser cleaning, the more important role of the focused laser beam technique here is its use in facilitating the thinning down of WSe_2 nanoflakes and in modifying the physical properties of WSe_2. Figure 4.3.2 shows optical images of the same area before and after laser modification. The visible optical contrast is a quick indication that the layer number has decreased after laser modification. In general, brighter higher contrast regions represent a thicker area and vice versa[33].

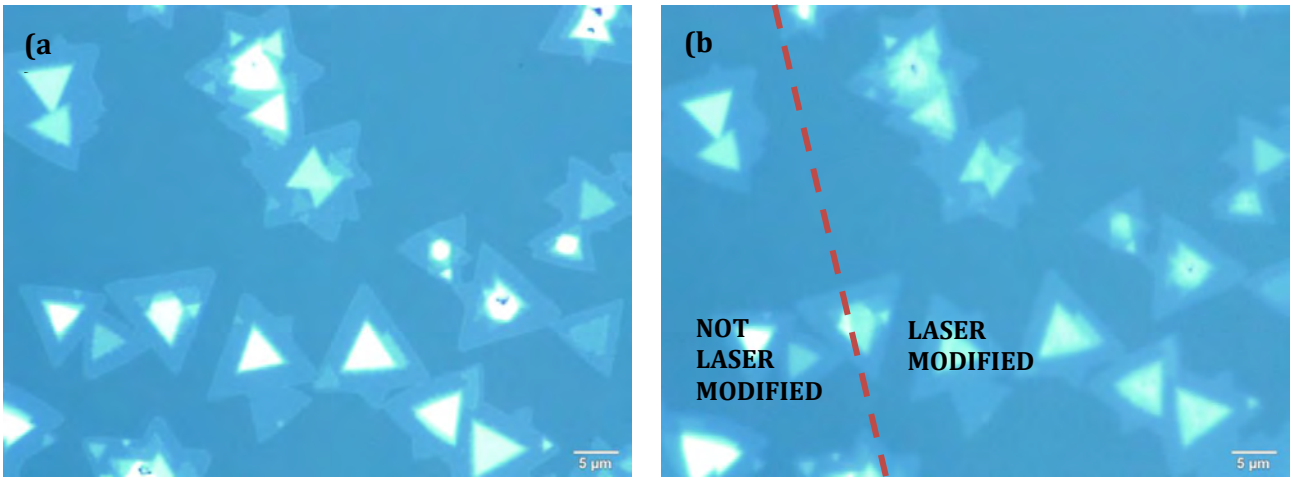

Figure 4.3.2: Optical Image of WSe_2 (a) Before laser modification (b) After laser modification

This is confirmed under SEM as shown in Figure 4.3.3. There is a visible change before and after laser modification in which the laser modified WSe_2 triangles appear more blurred out. The insets in the figure show a zoom-in of the respective regions. The bottom right hand region has been laser modified with a power density of 220mW/µm^2 at a speed of 20µm/s.

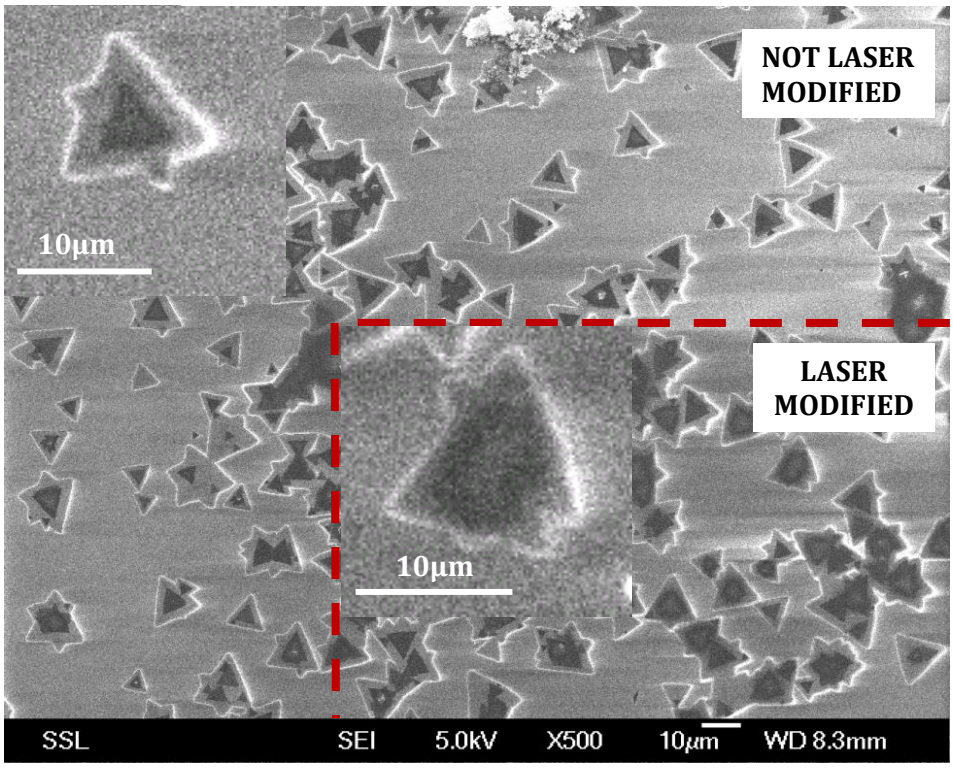

Figure 4.3.3: SEM image of laser modified region
Insets show enlarged image of WSe_2 triangle before and after laser modification.

The blurring out of the images may be due to the destruction of the thicker layers caused by high energy laser induced sublimating or melting. Laser irradiation in ambient conditions may also induce a thermal annealing effect which may introduce defect states below conduction band or above the valence band to the surface of WSe_2[34]. As seen in Figure 4.3.3, the darker regions become more smudged out and occupy a larger area after laser modification. The darker region represents a larger thickness, which corresponds to a smaller band gap due to quantum confinement effects[35]. This suggests that the WSe_2 flakes may become more conductive after laser modification.

When the same power of laser is used to quickly run through the WSe_2 triangles, parts of the triangle can be thinned down to a lower number of layers. This could be because of the lack of time for heat dissipation during this quick process. This is seen in Figure 4.3.4. The precise thickness will be confirmed through AFM.

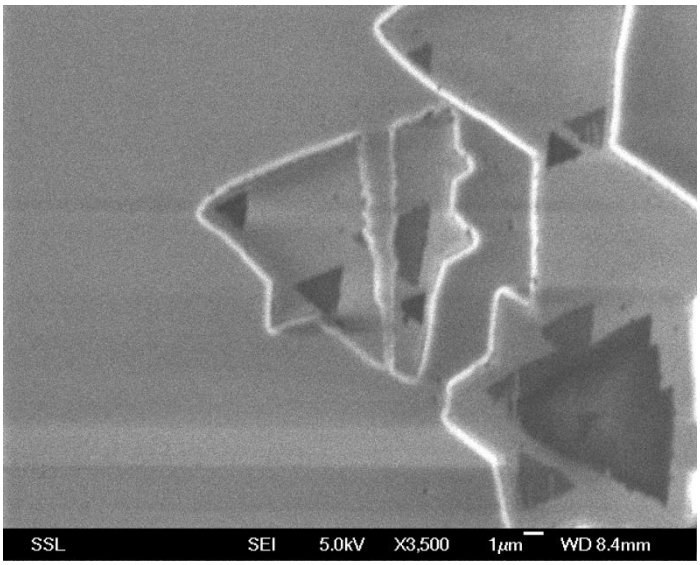

Figure 4.3.4: SEM image of quickly laser cut WSe_2 triangle

4.3.2 Raman Spectra and Mapping

The Raman spectra of the WSe_2 triangular flakes after laser modification show that there is no shift in the peak position before and after laser modification is

performed, as seen in Graph 4.3.2. The inset shows where the individual spectrum is obtained.

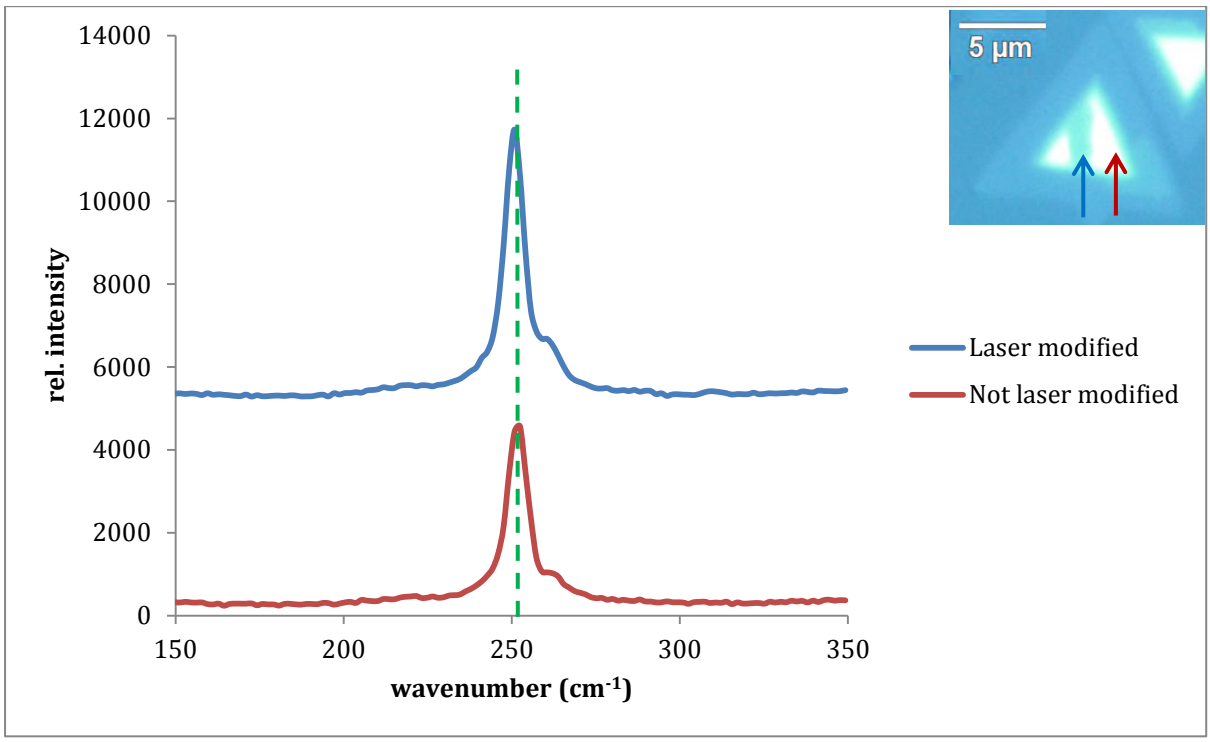

Graph 4.3.2: Raman Spectrum of WSe_2 flake (blue: laser modified, vertically displaced by 5000; red: as-synthesised). Inset shows the region where the spectrum was taken.

This is confirmed by Raman mapping performed at a window of 250-252 cm^{-1}. The uniform colour seen in the Raman mapping image (in peak position mode) of the laser modified flake in Figure 4.3.5 shows that the peak in the range of 250-252cm^{-1} corresponding to the out-of-plane E_{2g} mode of WSe_2 still exists after laser modification.

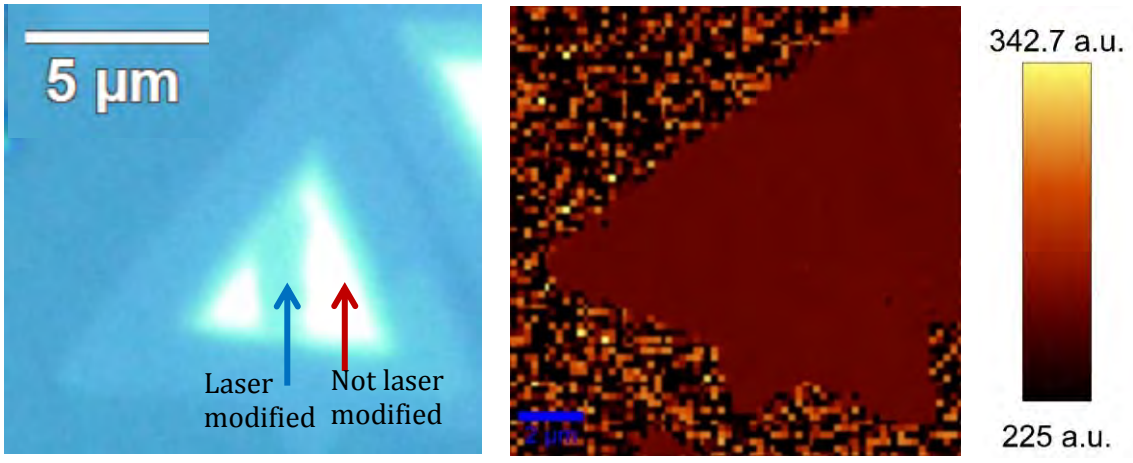

Figure 4.3.5: Raman peak position mapping of WSe_2 flake in the range of 250-252cm^{-1}

It can be observed, however, that the peak height of the laser cut region has increased (Graph 4.3.2). Using the same laser settings, the height of the Raman peaks is usually proportional to the absorptivity of the molecules, the polarisability of the sample, the amount of Raman-active modes which corresponds to concentration of Raman-active molecules and the thickness of the sample[36]. However, it is not possible that the WSe_2 flake has increased in thickness after laser cutting. This is confirmed by AFM scans which show that the flake has decreased in thickness after laser cutting (Section 4.3.3).

Perhaps, there has been an increase in crystalline quality. The width of a Raman peak is often used as a check of crystalline quality, where a narrower peak refers to a higher crystalline quality[37]. Graph 4.3.3 compares the full width half maximum (FWHM) of the peaks before and after laser has been used to cut through the WSe_2 flake. The Raman peaks have been fitted with a Gaussian-Lorentzian peak and the main peak at 250cm^{-1} has its FWHM reduced from 7.81 to 6.80 after laser modification, confirming the increased crystal quality after laser modification.

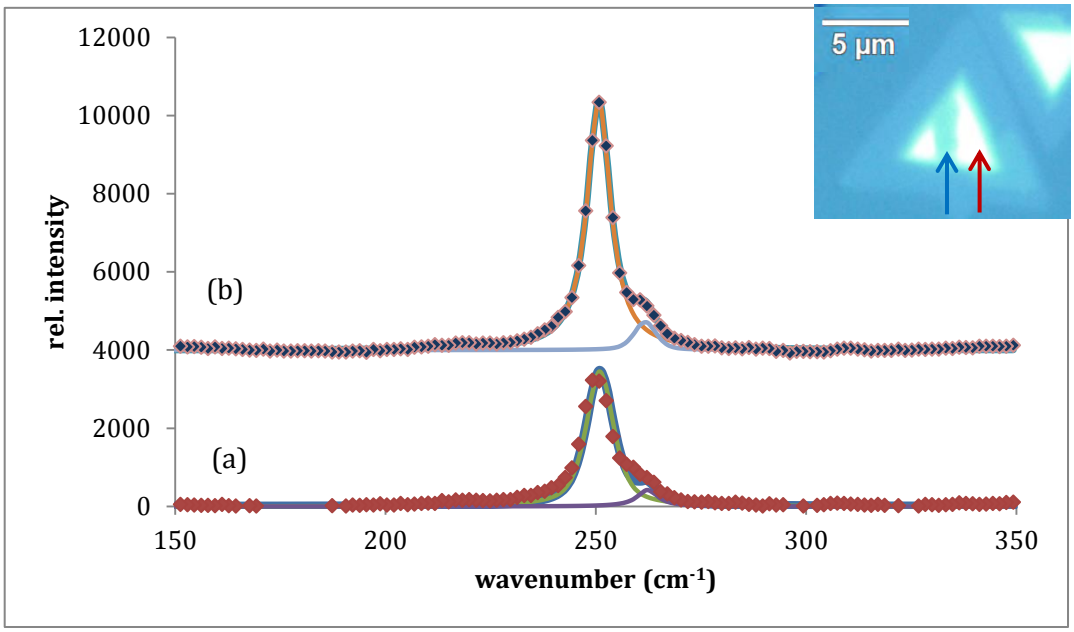

Graph 4.3.3: FWHM of Raman peaks in (a) As-synthesised (b) laser modified region Inset shows the region where the spectra are taken.

4.3.3 AFM Images

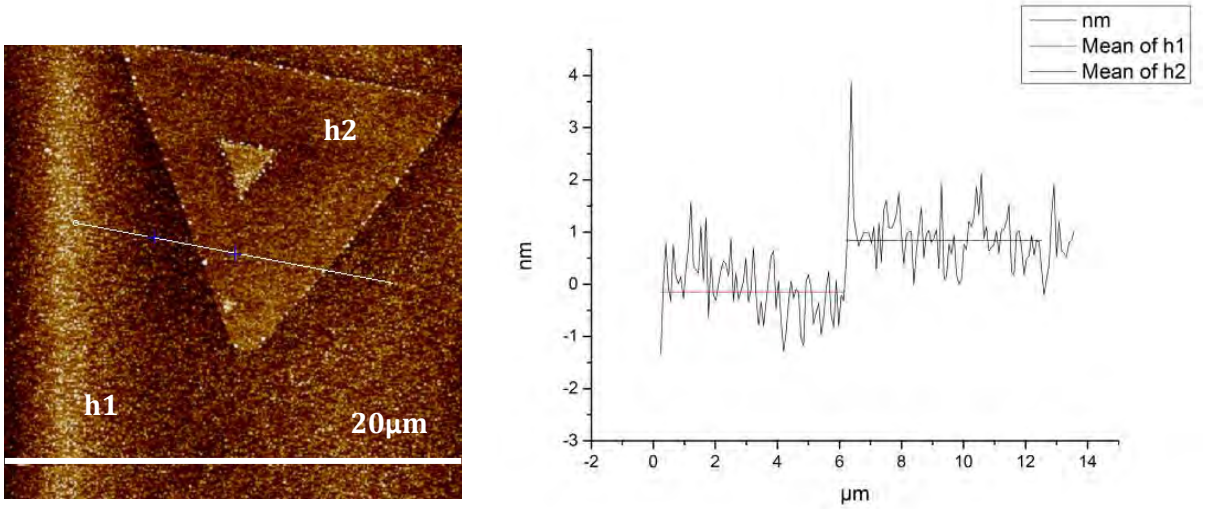

Figure 4.3.6: AFM image and step heights of monolayer WSe_2 flake

The vertical step height h2-h1 is measured with respect to the sapphire area outside the WSe_2 flake (WSe_2 absent). The step height is 0.9nm which correspond to ~ 1 monolayer (Figure 4.3.6).

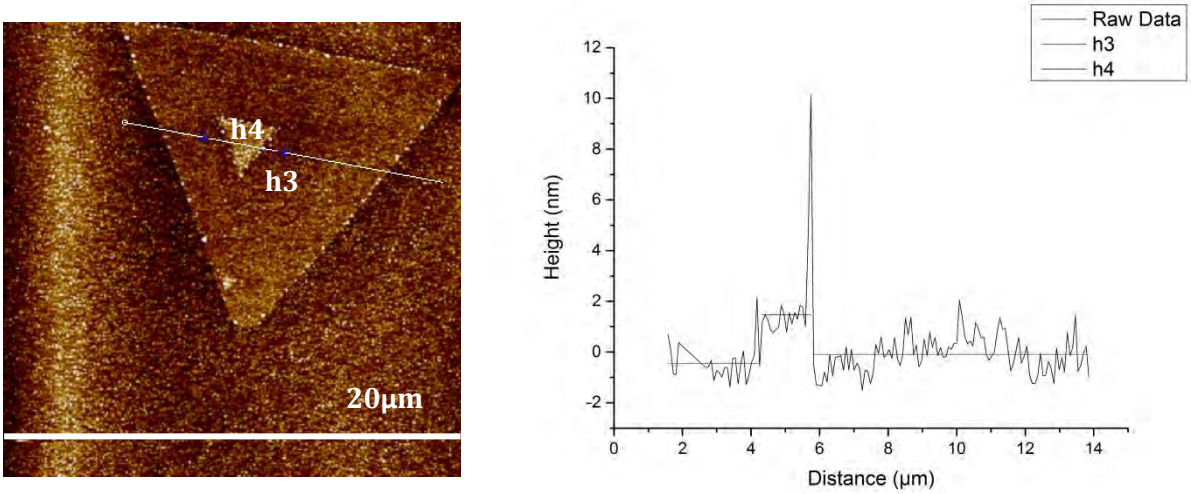

Figure 4.3.7: AFM image and step heights of triangular flake on top of WSe_2 monolayer

The vertical step height h4-h3 is measured to be 1.9nm which corresponds to ~ 3 monolayers. (Figure 4.3.7). This indicates that the smaller triangular flake is grown on top of the single monolayer in Figure 4.3.6.

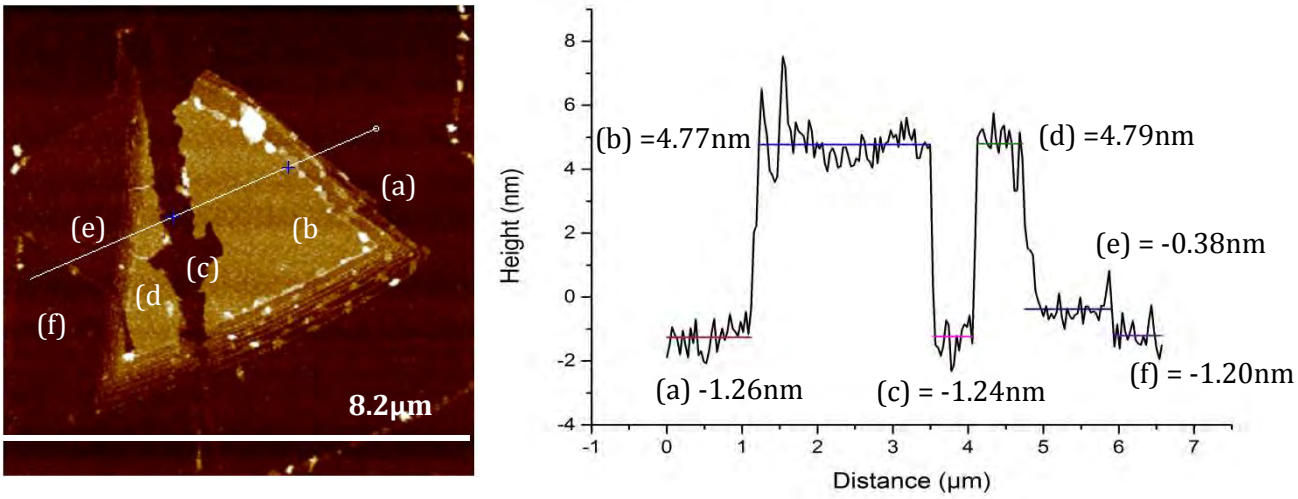

Figure 4.3.8: Step Height of Laser Cut WSe_2 nanoflake

After laser modification, comparing to the substrate (region (f)), the height analysis shows that the laser cutting has reduced the number of layers of WSe_2. This is observed in Figure 4.3.8 where a line scan of the different step heights has been done. The laser has cut the thickness of WSe_2 down to region (c) from a thickness of about 8 monolayers in regions (b) and (d). Region (f) appears to be relatively higher compared to region (a) even though it does not contain any WSe_2. However, this could be because the substrate is not uniform in thickness and may vary in height across the line scan.

The AFM data shows that the thickness of the WSe_2 nanoflake may be lowered by laser and post-synthesis systematic control of layer thickness of WSe_2 via laser thinning may be explored in future work. (Section 5.2)

4.3.4 XPS

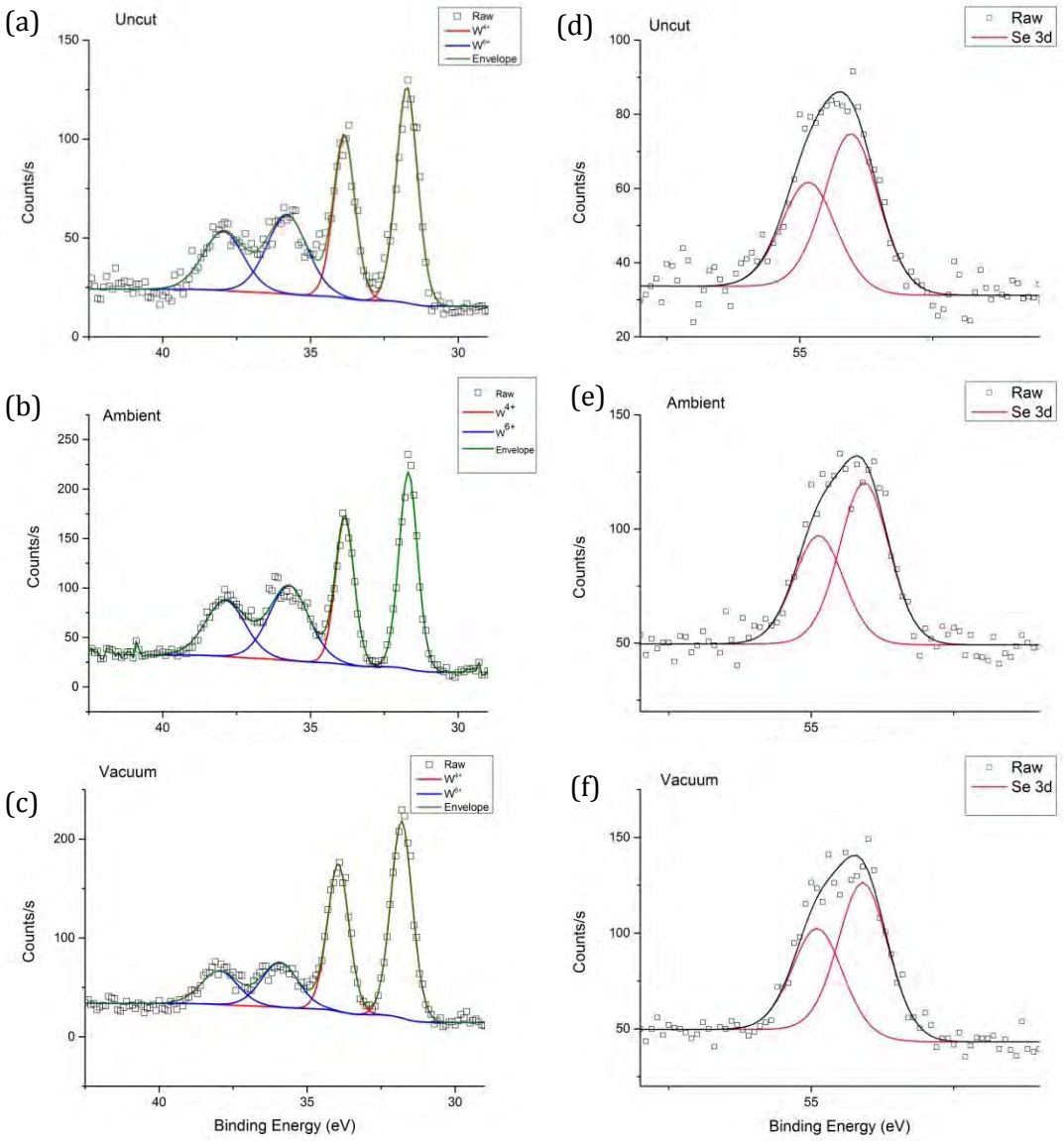

Graph 4.3.4: XPS scans in as-synthesised WSe_2 sample, and sample after laser modification in ambient and vacuum conditions (a)-(c) W4f (d)-(f) Se 3d

Graphs 4.3.4 (a) to (c) show the binding energy profiles obtained in a window from 27.5 – 44.5 eV which correspond to the W4f orbital. Graphs 4.3.4 (d) to (f) show the XPS scans obtained in a window from 51.0 – 58.0 eV which correspond to the Se3d orbital. The XPS peaks are analysed and fitted after a Shirley background subtraction. The binding energy values of W4f and O1s peaks are measured with respect to the C1s peak at 285.0eV. In the W4f peak fitting, the doublets are constrained by the peak

separation of 2.15eV[38] and area ratio of 0.75 due to the spin-orbit splitting theory of 4f levels. In the Se3d peak fitting, the doublets are constrained by peak separation of 0.8eV[39] and area ratio of 0.67 due to the spin-orbit splitting theory of 3d levels. The peaks follow a 70% Gaussian 30% Lorentzian fit.

In the W4f spectra seen in Graph 4.3.4 (a) to (c), 2 doublets may be observed. The first doublet at ~33.85/31.70eV corresponds to the $4f_{5/2}$ and $4f_{7/2}$ W^{4+} in W-Se environment[40]. The second doublet consists of weaker peaks at ~38.00/35.85eV, which corresponds to $4f_{5/2}$ and $4f_{7/2}$ W^{6+} in the W-O environment. This is in alignment with the values obtained for electrodeposited WO_3 (37.6/35.4eV), vacuum-deposited WO_3 and WO_3 powder, (38.2/36.0eV)[41, 42]. The second doublet can be associated with the presence of WO_3 which may be caused by the occasionally deposited WO_3 particles on the surface of the WSe_2 flakes. From SEM images in Figure 10, the formation of some particles at the edges of the WSe_2 triangles is observed. These could be WO_3 particles which form on the surface during the synthesis. The broadening of the FWHM of the W^{6+} peaks compared to the W^{4+} peaks suggests a change in the stoichiometry of the sample surface, which could be associated with the presence of some kind of defect states of WO_x (37.9/35.7eV)[43], where W may possess mixed oxidation states. Substoichiometric WO_{3-x} which contains W^{5+} (36.95/34.8eV) may also be present. However, this cannot be easily resolved.

The ratios of the areas corresponding to W^{6+} bonds to the areas for the all W4f bonds (including W-Se bonds), $\frac{W^{6+}}{W^{6+}+W^{4+}}$, are calculated to give 0.395 ± 0.002, 0.449 ± 0.002, and 0.279 ± 0.001 for as-synthesised regions, laser cut under ambient conditions, and laser modified in vacuum regions respectively (Table 4.3.1). Comparing against the as-synthesised regions, there is an increase in the ratio of WO_3 when the sample is laser modified under ambient conditions. This suggests a laser-induced oxidation in which

the oxygen available in the ambient environment reacts to oxidise WSe_2 into WO_3. Since the $\frac{W^{6+}}{W^{6+}+W^{4+}}$ ratio increases in the ambient condition compared to in the as-synthesised area of the WSe_2 sample, it could mean that more oxygen has been introduced into the film. This decreases the electronic density near the adjacent W atom, decreasing the screening effect and increasing the W4f binding energy[44]. This is observed in the XPS scan as the peak value for $4f_{7/2}$ W^{6+} increases from 35.85eV in as-synthesised, to 35.92eV and 36.23eV after laser modification in vacuum and ambient conditions respectively.

	Binding Energy of W^{4+} (eV)	**Binding Energy of W^{6+} (eV)**	$\frac{W^{6+}}{W^{6+}+W^{4+}}$
As-synthesised	33.88/31.73	38.00/35.85	0.395
Laser modified in **ambient** condition	33.84/31.69	37.88/36.23	0.449
Laser modified in **vacuum** condition	33.95/31.80	38.07/35.92	0.279

Table 4.3.1: Binding Energy of W^{6+} and Area ratio of W^{6+} and W^{4+}

The relative atomic concentrations between W^{4+} to Se were calculated via dividing the total peak area of W^{4+}4f and Se3d by the appropriate relative sensitivity factors. The stoichiometric ratio is the lowest in the pre-laser modified situation (1:1.81) and increases when laser modified in the ambient and vacuum conditions (1:2.05 and 1:2.06 respectively). This suggests an increase in quality of WSe_2 films after laser modification, which was seen earlier in Section 4.3.2 where the FWHM of the Raman peaks were found to have decreased after laser modification.

4.4 Optoelectronic Properties of WSe_2/sapphire

A two-terminal photodetector device based on WSe_2 nanoflakes on a sapphire substrate was fabricated (Figure 3.4.1). The distance between the 2 Ti/Au electrodes is 5μm.

4.4.1 I-V Curves

The I-V curves of the Ti/Au-WSe_2 flake-Ti/Au device are taken. The curves under dark condition and under a broad laser beam of wavelength 543.5nm (energy ~ 2.3eV) and incident laser power 3.63mW (spot size~3mm, power density~5.14×10^{-7}mW/μm^2) are shown in Graph 4.4.1. The voltage is swept from -5V to +5V. Semiconductors often show higher conductivity when excited by photons of energy greater than the band gap of the material[45]. This laser wavelength has energy higher than the band gap of WSe_2 (energy ≈ 1.2eV for bulk WSe_2 and 1.64eV for monolayer WSe_2).

The WSe_2 flake connected to Ti/Au electrodes at both ends may be modelled as a circuit with two Schottky junctions connected back to back in series[46]. When an external bias is applied, one of the Schottky junctions becomes forward biased and the other reverse biased. The work functions of Ti (4.3eV) and Au (5.1eV)[47] are slightly higher than that of bulk and monolayer WSe_2 (3.9eV and 4.3eV respectively)[22]. When the metal electrode and WSe_2 are in contact, there is Fermi level alignment, causing band bending and a Schottky barrier to be formed. The barrier height is the difference between the metal work function and electron affinity of the semiconductor. Large band gap semiconductors like WSe_2 are known for their difficulties in forming ohmic contacts. Ti forms Schottky barrier near the middle of the WSe2 band gap, and exhibits low current ambipolar characteristics[7]. This is seen in Figure 4.4.1.

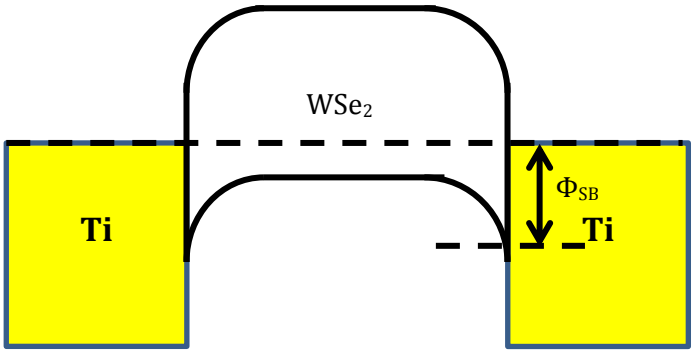

Figure 4.4.1: Ti WSe_2 contact (Φ_{SB} = Schottky barrier height)

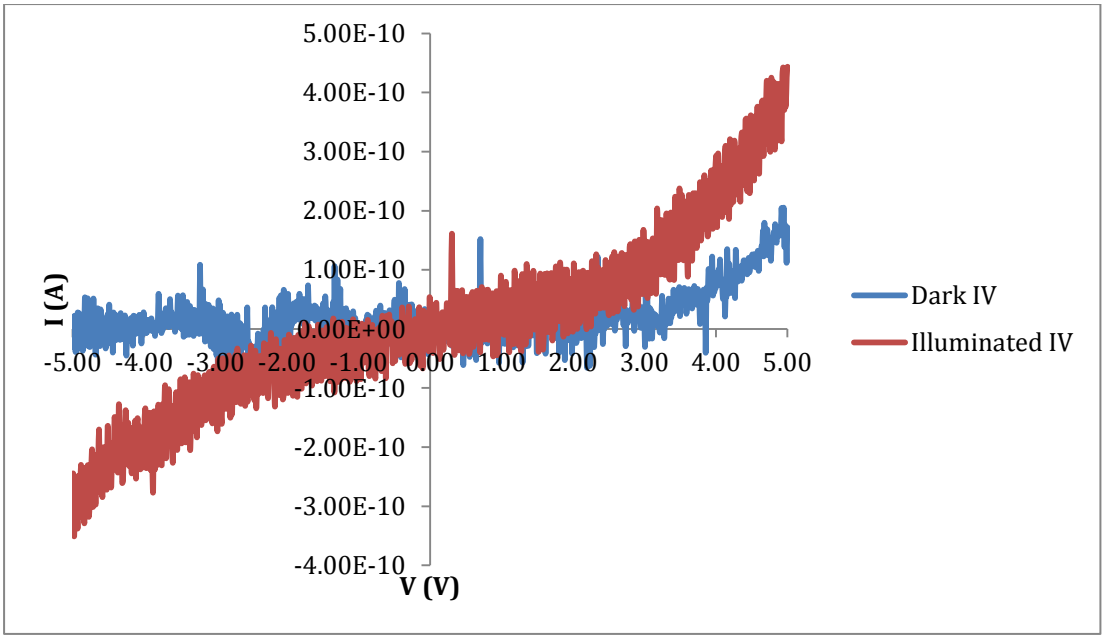

Graph 4.4.1: Dark I-V and I-V curve under laser illumination (before laser modification)

The I-V curves (Graph 4.4.1) obtained in this experiment exhibit an asymmetrical and nonlinear response under positive and negative bias. The nonlinear response indicates that the photocurrent is dominated by Schottky barrier formation between the metal electrodes and WSe_2. The asymmetric response may be attributed to the contact area differences, where different widths of the WSe_2 flake are in contact with each electrode. It may also be attributed to the varying thickness of the flake in contact with each electrode. The band gap of WSe_2 differs depending on the thickness of the flake[11]. The two above mentioned factors may cause the WSe_2 flake contacting the electrode to form two uneven Schottky barriers due to different coupling (Figure 4.4.1), leading to the asymmetric I-V characteristic. In this device, the current is more dominant when positive voltage is applied.

The increase in current after the laser is shone onto the device is good motivation to investigate photocurrent characteristics in Section 4.4.2.

4.4.2 Laser modification under ambient conditions

The gold electrodes before and after laser modification are shown in Figure 4.4.2 (a) and (b) respectively. The optical contrast before and after the electrodes were laser modified can be observed, where the WSe_2 flakes after laser modification show a lower contrast. This is similar to what was observed in Section 4.2. Shown in the dashed line boxes are the WSe_2 flakes in contact with both electrodes that act as the conducting channel.

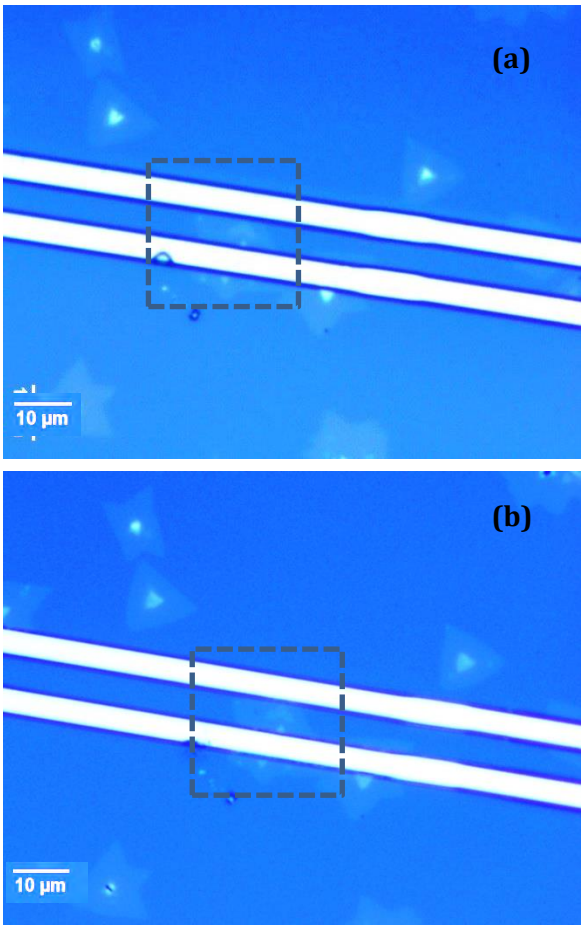

Figure 4.4.2: Optical Images of WSe_2 triangles between Ti/Au electrodes (a) Before laser modification (b) After laser modification.

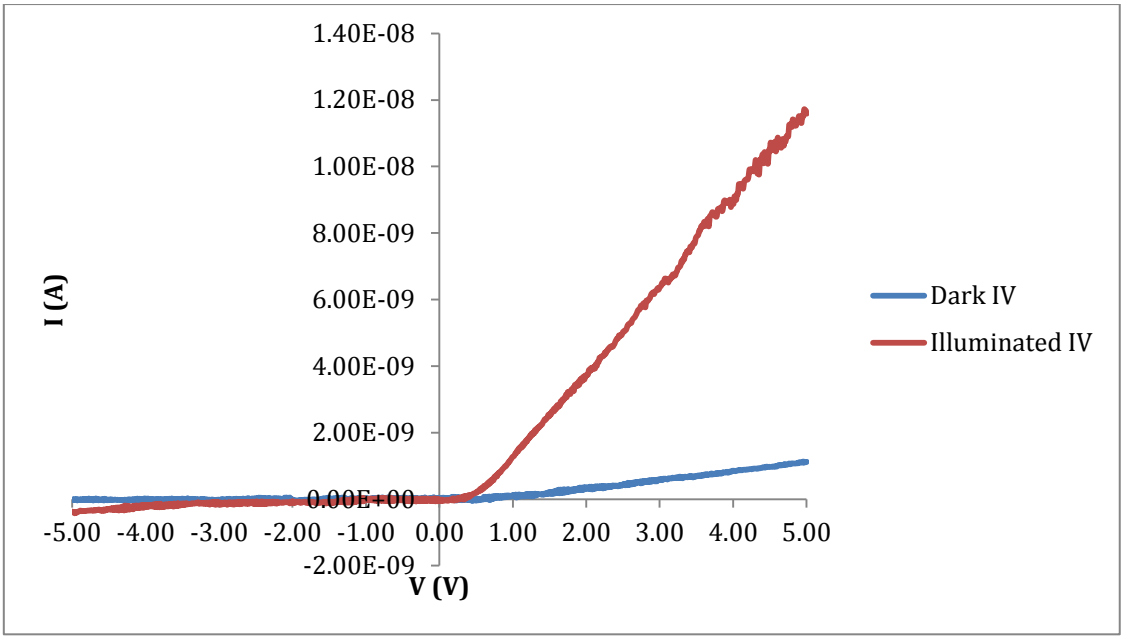

Graph 4.4.2: Dark I-V and I-V curve under laser irradiation (after laser modification)

Graph 4.4.2 shows both dark I-V and I-V curves under laser illumination after laser modification. The curves both exhibit a Schottky diode-like behaviour. The asymmetric response of positive and negative applied voltage is more obvious after laser modification.

The observed photocurrent seen in Graph 4.4.1 and 4.4.2 could be attributed to electron-hole pairs which are generated in the samples. These electron-hole pairs are separated under the applied bias and then collected at the metal electrodes. Before laser modification (Graph 4.4.1), under illumination by laser, the turn on voltage is ~1V as opposed to ~2.6V in a dark condition. Similarly, after laser modification (Graph 4.4.2), under laser illumination, the turn on voltage is ~0.5V as opposed to ~1V in a dark condition. The laser helps to excite the charge carriers to overcome the Schottky barriers to generate a photocurrent.

The origin of the photocurrent may be attributed to many factors, including thermal effects due to the laser irradiation. This results in thermoelectric effects at the WSe_2-metal electrode contact. Thermalisation increases the energy of the charge

carriers in the WSe_2 flake, which gain greater velocities than those in the metal, causing them to diffuse into the electrode. The photocurrent may also have originated from the intrinsic response of the WSe_2 flake itself. To study the mechanism behind the photocurrent, focused laser irradiation can be done in future work. This is discussed in Section 5.2.

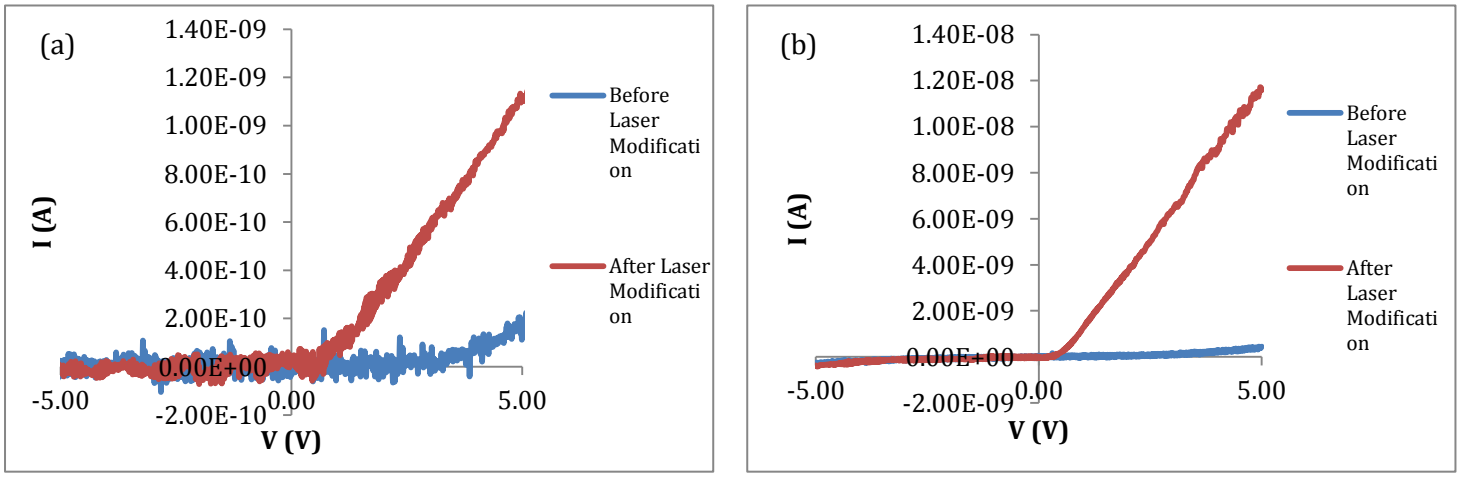

Graph 4.4.3: I-V curves before and after laser modification (a) Dark I-V (b) I-V under illumination

Comparing the magnitude of both dark current and photocurrent before and after laser modification, it is observed that there is an increase one order of magnitude of both currents after laser modification (Graph 4.4.3 (a) and (b)). This phenomenon may be attributed to introduction of defect states within the band gap. This has previously been reported in literature, where irradiation with α particles which have energies in the MeV range and thermal annealing introduce anion vacancies in MoS_2, $MoSe_2$ and WSe_2. These vacancies create sub band gap energy levels about 0.2 eV below the band edge. When laser is shone onto the sample, free charge carriers are released to or from the defect states due to laser irradiation and/or laser-induced thermal heating. Under the external bias, the charge carriers are separated and their motion leads to the observed photocurrent. According to Sefaattin et al., the effect of these irradiation techniques is not observed under vacuum conditions, and this suggests that the

interaction with ambient gas molecules which may be physically adsorbed at the defect sites is important[34, 48].

In our experiment, one such ambient gas molecule is probably O_2, which oxidises WSe_2 to WO_3, as discussed in the XPS results (Section 4.3.4). The XPS results show that after laser modification in ambient conditions, the ratio of W^{6+} in the WO_3 environment increases. The XPS scans also suggest the presence of mixed WO_x defect states. Sub-stoichiometric tungsten oxides WO_{3-x} have shown metallic character which may enhance charge transport[49]. WO_3 nanocrystalline particles introduced into amorphous carbon has shown increases in electrical conductivity[50]. Similarly, the introduction of WO_3 and WO_x defect states may contribute to the increase in current seen after laser modification in ambient conditions.

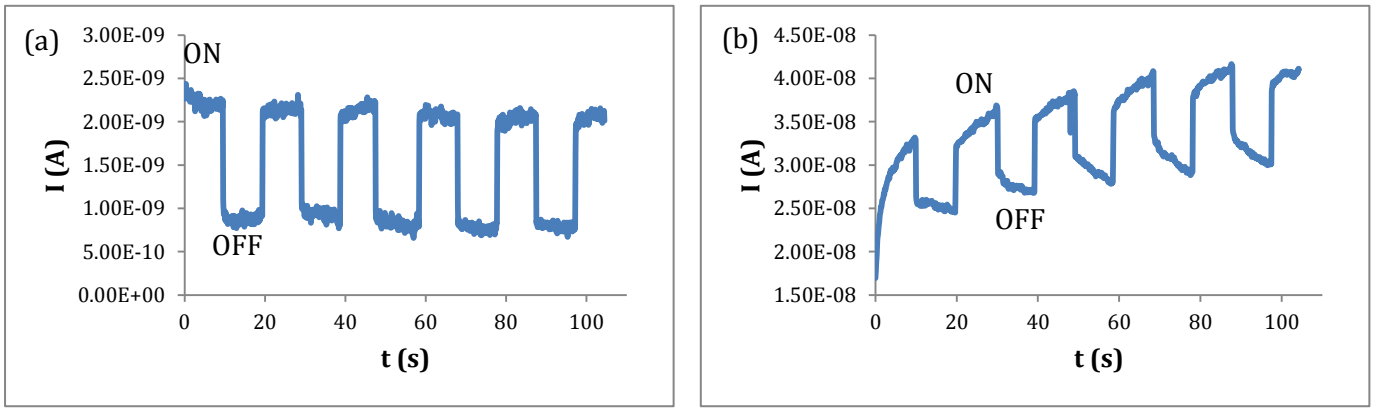

Graph 4.4.4: Photocurrent response of WSe_2/sapphire device under +6V applied bias (a) Before laser modification (b) After laser modification

Graph 4.4.4 (a) and (b) show the time-resolved photocurrent response of the device in the ON-OFF states before and after laser modification respectively under a +6V bias. Before laser modification, the device showed a rapid photoresponse with ~ 163% ($I_{photo} - I_{dark} / I_{dark} \times 100\%$) is observed. After laser modification, the device shows a photo response with both rapid and slowly varying parts and a ~ 36% current increase. The photocurrent shows a characteristic rapid rise followed by a slow rise and a rapid drop followed by a slow decay when the laser is "off".

Three comparisons can be made of the device before and after laser modification: (1) After laser modification, the value of photocurrent ($\sim 10^{-8}$ A) has increased by an order of magnitude from the value before laser modification ($\sim 10^{-9}$ A) (2) After laser modification, there is a gradual increase in value of current in the "off" state as time goes on. The current never reaches the current in the initial "off" state. This is in contrast with before laser modification where the current returns to a value comparable to its dark current when the device is in its "off" state. (3) After laser modification, the time response shows a sharp rise followed by a slow rise and a sharp drop followed by a slow decay as opposed to sharp rises and drops before laser modification when the laser is turned on and off.

The origin of the increase in magnitude of photocurrent was proposed earlier to be due to the introduction of defect states within the band gap of WSe_2.

The gradual increase in value of dark current is due to the laser-induced thermal heating. As time goes on, the heat absorbed by the carriers in the WSe_2 sample causes them to move faster and cause the dark current to increase. It could also be because of carrier trapping into various surface defect states, where there is not enough time for the photocurrent to decay to its initial "off" state current before the sample is irradiated again. This suggests that the total decay time is longer than the time allowed between the "on" and "off" states ($\sim$10s in this experiment).

The device after laser modification exhibits a slow rise in photocurrent. This may be attributed to various factors such as the laser-induced thermal heating, carrier trapping and interaction of surface states with the laser[51]. It also exhibits a fast then a relatively slower decay of photocurrent when the laser is switched to the "off" state. The fast decay is associated with the absence of photo excitation after the laser is off.

To determine the time constant associated with the slow rise and decay of current, we may use the rate equations (1) and (2) respectively:

$$\frac{dI(t)}{dt} = G - \frac{I}{\tau}\ s \quad (1) \qquad and \qquad \frac{dI(t)}{dt} = \frac{-I}{\tau} \qquad (2)$$

Equation (1) and (2) give (3) and (4) respectively:

$$\mathrm{I(t)} = I_i\left(1 - e^{-\frac{t}{\tau}}\right) \quad (3) \quad and \quad \mathrm{I(t)} = I_i e^{-\frac{t}{\tau}} \quad (4)$$

where I_i refers to the initial current and τ is the time constant. The experimental data for the slow rise and decay curve fits well with this model (equations (1) to (4)), and the fitted equation takes the form:

$$I(t) = I_0 + A(1 - e^{-\frac{t-t_0}{\tau}}) \qquad (5)$$

$$I(t) = I_0 + Ae^{-(t-t_0)/\tau} \qquad (6)$$

In equation (5) and (6), t is the final response time, t_0 is the initial response time, I_0 is the dark current and A is the amplitude of current.

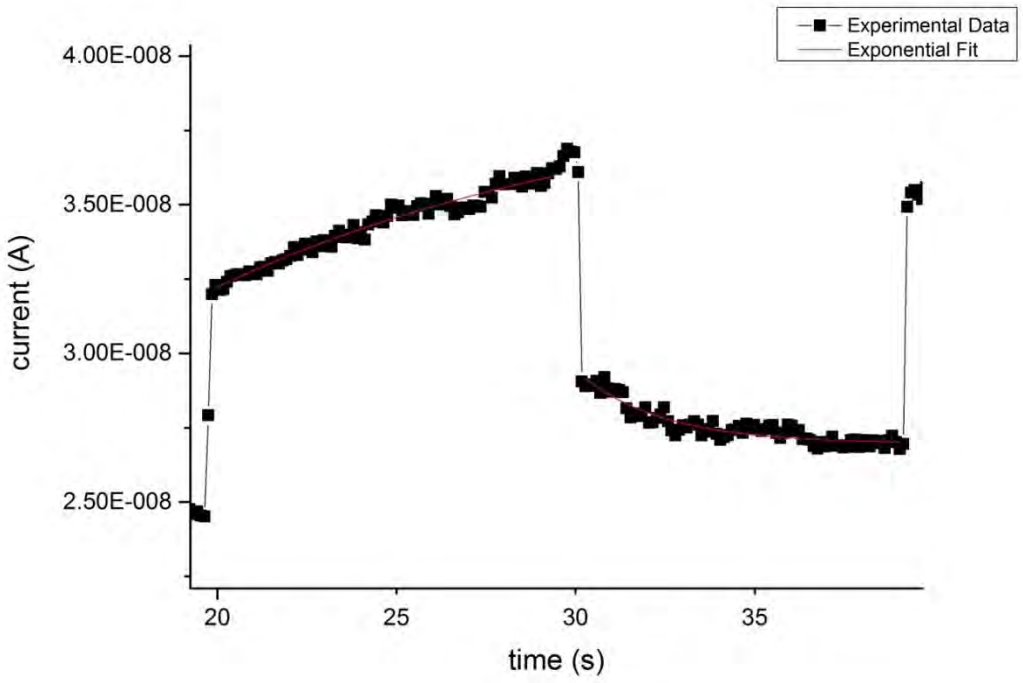

Graph 4.4.5: Exponential fitting of slow rise and decay curves

From the exponential fit (one “on” and “off” cycle is presented in Graph 4.4.5), the rise time ranges from $\sim$ 6 – 10 s and the decay time ranges from $\sim$ 2 – 11 s. Both rise and decay times are slow, and it may be due to the trapping of photogenerated charge carriers into surface defect states. For the decay time, it increases as time passes. As the laser irradiates the sample for a longer time, more carriers are excited into a non-equilibrium state: they do not undergo recombination as readily. The carriers remain as free carriers and cause the dark current to increase in value. As the dark current is of a higher value, it takes longer to reduce to its original value. Therefore, the decay time increases.

Chapter 5

5 Conclusion

5.1 Summary of Project

First, large-area uniform layers of WSe_2 have been synthesized via the chemical vapour deposition technique. This was done by optimising the conditions in the tube furnace and introducing hydrogen into the gas flow to act as a reducer. Flake sizes of up to 30μm were found to be form, and the size and nucleation density of the WSe_2 flakes were found to depend largely on the substrate temperature.

Next, post-synthesis laser scanning was done on the synthesised WSe_2 flakes. Characterisation done on WSe_2 after laser modification in ambient conditions revealed interesting changes in physical and chemical properties. Firstly, laser scanning allowed us to reduce the thickness of the WSe_2 flakes. The crystalline quality of the WSe_2 flakes was also found to have increased after laser modification. On the surface, WO_3 and other defect states of WO_x appeared to have increased after laser modification possibly due to the oxidation of WSe_2 in ambient conditions.

Finally, a photodetector device based on the WSe_2 nanoflakes was fabricated by depositing two terminal Ti/Au electrodes. The device showed asymmetric and non-linear I-V characteristics which may be attributed to the formation of uneven Schottky barrier contacts between the WSe_2 flake and the electrode. It showed photocurrent response under global laser irradiation. The photocurrent increased in magnitude after laser modification in ambient conditions. This increase may be associated with the introduction of WO_x-related defect states within the WSe_2 band-gap. Also, I-t characteristics with rapidly and slowly varying components were found after laser modification. We suggested some possibilities for the observed I-t characteristics, which

include trapping into defect states and thermal heating induced by laser irradiation. More work has to be done to understand the mechanism behind the photocurrent after laser modification.

5.2 Future Directions

Since it was found that it is possible to reduce the layer thickness of WSe_2 flakes using laser irradiation, it should also be possible to engineer different thickness flakes by adjusting the incident laser power density on the WSe_2 flakes. It would be interesting to note which laser powers are more effective in thinning down the WSe_2 flakes. This is a useful technique to create on-demand monolayer WSe_2 for use in optoelectronic devices.

Due to time constraint, it was not possible to conduct the photocurrent testing after laser modification in vacuum conditions. The ratio of W^{6+} decreases after laser modification in vacuum. Perhaps, electrons could be trapped at these defect states, leaving the holes unpaired and thus able to contribute to photocurrent. In the ambient condition, oxygen related gas molecules in the air may occupy the defect states, rendering them unable to contribute to photocurrent[52]. In vacuum condition, however, there is the reduction of the presence of ambient gas molecules which can occupy these defect states. Hence, there may be an increase in the magnitude of photocurrent observed. Also, in ambient conditions, the presence of air can help to dissipate some heat generated by the laser and thus laser-induced thermal effects may be diminished. Laser modification under vacuum conditions can help to reduce these impeding factors and cause the WSe_2 to reach a higher temperature, leading to a possible additional increase in photocurrent[51].

To gain a better insight into the major contributing factors to the photocurrent, photocurrent measurements with localized focused laser irradiation can be carried on.

Under global irradiation, the detected photocurrent may be influenced by a number of factors, including the film-electrode interface barriers, the intrinsic response of the film or the carrier transport within the film. The focused laser beam spot can be positioned to irradiate different parts of the device, including the film-electrode interface and the film itself to study where the photo responses originate. It would also be good to conduct simulations and first-principle calculations of where the defect states lie with respect to the intrinsic band levels of WSe_2 to further ascertain the origins of the increased photocurrent after laser modification.

References

1. Wilson, J.; Yoffe, A., The transition metal dichalcogenides discussion and interpretation of the observed optical, electrical and structural properties. *Advances in Physics* 1969, 18, 193-335.
2. Wang, Q. H.; Kalantar-Zadeh, K.; Kis, A.; Coleman, J. N.; Strano, M. S., Electronics and optoelectronics of two-dimensional transition metal dichalcogenides. *Nature Nanotechnology* 2012, 7, 699-712.
3. Chhowalla, M.; Shin, H. S.; Eda, G.; Li, L.-J.; Loh, K. P.; Zhang, H., The chemistry of two-dimensional layered transition metal dichalcogenide nanosheets. *Nature chemistry* 2013, 5, 263-275.
4. Zeng, H. L.; Liu, G. B.; Dai, J. F.; Yan, Y. J.; Zhu, B. R.; He, R. C.; Xie, L.; Xu, S. J.; Chen, X. H.; Yao, W.; Cui, X. D., Optical signature of symmetry variations and spin-valley coupling in atomically thin tungsten dichalcogenides. *Scientific Reports* 2013, 3.
5. Zhao, W.; Ghorannevis, Z.; Chu, L.; Toh, M.; Kloc, C.; Tan, P.-H.; Eda, G., Evolution of electronic structure in atomically thin sheets of WS2 and WSe2. *ACS nano* 2012, 7, 791-797.
6. Das, S.; Appenzeller, J., WSe2 field effect transistors with enhanced ambipolar characteristics. *Applied Physics Letters* 2013, 103.
7. Fang, H.; Chuang, S.; Chang, T. C.; Takei, K.; Takahashi, T.; Javey, A., High-Performance Single Layered WSe2 p-FETs with Chemically Doped Contacts. *Nano Letters* 2012, 12, 3788-3792.
8. Huang, J.-K.; Pu, J.; Hsu, C.-L.; Chiu, M.-H.; Juang, Z.-Y.; Chang, Y.-H.; Chang, W.-H.; Iwasa, Y.; Takenobu, T.; Li, L.-J., Large-Area Synthesis of Highly Crystalline WSe2 Monolayers and Device Applications. *ACS Nano* 2013, 8, 923-930.
9. Li, H.; Lu, G.; Wang, Y.; Yin, Z.; Cong, C.; He, Q.; Wang, L.; Ding, F.; Yu, T.; Zhang, H., Mechanical Exfoliation and Characterization of Single- and Few-Layer Nanosheets of WSe2, TaS2, and TaSe2. *Small* 2013, 9, 1974-1981.
10. Liu, W.; Kang, J. H.; Sarkar, D.; Khatami, Y.; Jena, D.; Banerjee, K., Role of Metal Contacts in Designing High-Performance Monolayer n-Type WSe2 Field Effect Transistors. *Nano Letters* 2013, 13, 1983-1990.
11. Sahin, H.; Tongay, S.; Horzum, S.; Fan, W.; Zhou, J.; Li, J.; Wu, J.; Peeters, F. M., Anomalous Raman spectra and thickness-dependent electronic properties of WSe2. *Physical Review B* 2013, 87.
12. Xu, K.; Wang, Z. X.; Du, X. L.; Safdar, M.; Jiang, C.; He, J., Atomic-layer triangular WSe2 sheets: synthesis and layer-dependent photoluminescence property. *Nanotechnology* 2013, 24.
13. Jariwala, D.; Sangwan, V. K.; Late, D. J.; Johns, J. E.; Dravid, V. P.; Marks, T. J.; Lauhon, L. J.; Hersam, M. C., Band-like transport in high mobility unencapsulated single-layer MoS2 transistors. *Applied Physics Letters* 2013, 102, 173107.
14. Radisavljevic, B.; Radenovic, A.; Brivio, J.; Giacometti, V.; Kis, A., Single-layer MoS2 transistors. *Nature nanotechnology* 2011, 6, 147-150.
15. Yoon, Y.; Ganapathi, K.; Salahuddin, S., How good can monolayer MoS2 transistors be? *Nano letters* 2011, 11, 3768-3773.
16. Lee, H. S.; Min, S.-W.; Chang, Y.-G.; Park, M. K.; Nam, T.; Kim, H.; Kim, J. H.; Ryu, S.; Im, S., MoS2 nanosheet phototransistors with thickness-modulated optical energy gap. *Nano letters* 2012, 12, 3695-3700.
17. Lopez-Sanchez, O.; Lembke, D.; Kayci, M.; Radenovic, A.; Kis, A., Ultrasensitive photodetectors based on monolayer MoS2. *Nature nanotechnology* 2013, 8, 497-501.
18. Castro Neto, A. H.; Guinea, F.; Peres, N. M. R.; Novoselov, K. S.; Geim, A. K., The electronic properties of graphene. *Reviews of Modern Physics* 2009, 81, 109-162.
19. Han, M. Y.; Özyilmaz, B.; Zhang, Y.; Kim, P., Energy band-gap engineering of graphene nanoribbons. *Physical review letters* 2007, 98, 206805.
20. Huang, X.; Qi, X.; Boey, F.; Zhang, H., Graphene-based composites. *Chemical Society Reviews* 2012, 41, 666-686.

21. Lembke, D.; Kis, A., Correction to Breakdown of High-Performance Monolayer MoS2 Transistors. *ACS nano* 2013, 7, 3730-3730.
22. Britnell, L.; Ribeiro, R.; Eckmann, A.; Jalil, R.; Belle, B.; Mishchenko, A.; Kim, Y.-J.; Gorbachev, R.; Georgiou, T.; Morozov, S., Strong light-matter interactions in heterostructures of atomically thin films. *Science* 2013, 340, 1311-1314.
23. Baugher, B. W.; Churchill, H. O.; Yang, Y.; Jarillo-Herrero, P., Optoelectronic devices based on electrically tunable pn diodes in a monolayer dichalcogenide. *Nature nanotechnology* 2014.
24. Kuc, A.; Zibouche, N.; Heine, T., Influence of quantum confinement on the electronic structure of the transition metal sulfide T S 2. *Physical Review B* 2011, 83, 245213.
25. Smith, D., *Thin-Film Deposition: Principles and Practice*. McGraw-Hill Education: 1995.
26. Lee, Y. H.; Zhang, X. Q.; Zhang, W.; Chang, M. T.; Lin, C. T.; Chang, K. D.; Yu, Y. C.; Wang, J. T. W.; Chang, C. S.; Li, L. J., Synthesis of Large‐Area MoS2 Atomic Layers with Chemical Vapor Deposition. *Advanced Materials* 2012, 24, 2320-2325.
27. Liu, K.-K.; Zhang, W.; Lee, Y.-H.; Lin, Y.-C.; Chang, M.-T.; Su, C.-Y.; Chang, C.-S.; Li, H.; Shi, Y.; Zhang, H., Growth of large-area and highly crystalline MoS2 thin layers on insulating substrates. *Nano letters* 2012, 12, 1538-1544.
28. Jäger-Waldau, A.; Lux-Steiner, M.; Jäger-Waldau, R.; Burkhardt, R.; Bucher, E., Composition and morphology of MoSe< sub> 2</sub> thin films. *Thin Solid Films* 1990, 189, 339-345.
29. Li, H.-M.; Lee, D.-Y.; Choi, M. S.; Qu, D.; Liu, X.; Ra, C.-H.; Yoo, W. J., Metal-Semiconductor Barrier Modulation for High Photoresponse in Transition Metal Dichalcogenide Field Effect Transistors. *Scientific reports* 2014, 4.
30. Lu, X.; Utama, M. I. B.; Zhang, J.; Zhao, Y. Y.; Xiong, Q. H., Layer-by-layer thinning of MoS2 by thermal annealing. *Nanoscale* 2013, 5, 8904-8908.
31. Liu, Y. L.; Nan, H. Y.; Wu, X.; Pan, W.; Wang, W. H.; Bai, J.; Zhao, W. W.; Sun, L. T.; Wang, X. R.; Ni, Z. H., Layer-by-Layer Thinning of MoS2 by Plasma. *Acs Nano* 2013, 7, 4202-4209.
32. Castellanos-Gomez, A.; Barkelid, M.; Goossens, A. M.; Calado, V. E.; van der Zant, H. S. J.; Steele, G. A., Laser-Thinning of MoS2: On Demand Generation of a Single-Layer Semiconductor. *Nano Letters* 2012, 12, 3187-3192.
33. Li, H.; Wu, J. M. T.; Huang, X.; Lu, G.; Yang, J.; Lu, X.; Zhang, Q. H.; Zhang, H., Rapid and Reliable Thickness Identification of Two-Dimensional Nanosheets Using Optical Microscopy. *Acs Nano* 2013, 7, 10344-10353.
34. Sefaattin, T.; Joonki, S.; Can, A.; Wen, F.; Alexander, L.; Jeong Seuk, K.; Jonathan, L.; Changhyun, K.; Rajamani, R.; Jian, Z.; Frank, O.; Jingbo, L.; Jeffrey, C. G.; Junqiao, W., Defects activated photoluminescence in two-dimensional semiconductors: interplay between bound, charged, and free excitons. *Scientific Reports* 2013, 3.
35. Solid-state physics, fluidics, and analytical techniques in micro- and nanotechnology, 3d ed. *Reference and Research Book News* 2011, 26.
36. Alexander, R. Advantages of Raman Spectroscopy when Analysing Materials Through Glass or Polymer Containers and in Aqueous Solution. http://www.perkinelmer.com/CMSResources/Images/APP_RamanAnalysisTthrougGlassPolymerAqueous.pdf (accessed 1 April).
37. Laskar, M. R.; Ma, L.; Kannappan, S.; Park, P. S.; Krishnamoorthy, S.; Nath, D. N.; Lu, W.; Wu, Y.; Rajan, S., Large area single crystal (0001) oriented MoS2. *Applied Physics Letters* 2013, 102, 252108.
38. Gogova, D.; Gesheva, K.; Szekeres, A.; Sendova-Vassileva, M., Structural and optical properties of CVD thin tungsten oxide films. *PHYSICA STATUS SOLIDI A APPLIED RESEARCH* 1999, 176, 969-984.
39. Wang, H.; Kong, D.; Johanes, P.; Cha, J. J.; Zheng, G.; Yan, K.; Liu, N.; Cui, Y., MoSe2 and WSe2 nanofilms with vertically aligned molecular layers on curved and rough surfaces. *Nano letters* 2013, 13, 3426-3433.

40. Grigoriev, S.; Fominski, V. Y.; Gnedovets, A.; Romanov, R., Experimental and numerical study of the chemical composition of WSe_x thin films obtained by pulsed laser deposition in vacuum and in a buffer gas atmosphere. *Applied Surface Science* 2012, 258, 7000-7007.
41. Su, L.; Zhang, L.; Fang, J.; Xu, M.; Lu, Z., Electrochromic and photoelectrochemical behavior of electrodeposited tungsten trioxide films. *Solar energy materials and solar cells* 1999, 58, 133-140.
42. Morar, J.; Himpsel, F.; Hughes, G.; Jordan, J.; McFeely, F.; Hollinger, G., High resolution photoemission investigation: The oxidation of W. *Journal of Vacuum Science & Technology A* 1985, 3, 1477-1480.
43. Leftheriotis, G.; Papaefthimiou, S.; Yianoulis, P.; Siokou, A., Effect of the tungsten oxidation states in the thermal coloration and bleaching of amorphous WO_3 films. *Thin solid films* 2001, 384, 298-306.
44. Ahsan, M.; Ahmad, M.; Tesfamichael, T.; Bell, J.; Wlodarski, W.; Motta, N., Low temperature response of nanostructured tungsten oxide thin films toward hydrogen and ethanol. *Sensors and Actuators B: Chemical* 2012, 173, 789-796.
45. Bube, R. H., *Photoelectronic properties of semiconductors*. Cambridge University Press: 1992.
46. Zhang, Z.; Yao, K.; Liu, Y.; Jin, C.; Liang, X.; Chen, Q.; Peng, L. M., Quantitative analysis of current–voltage characteristics of semiconducting nanowires: decoupling of contact effects. *Advanced functional materials* 2007, 17, 2478-2489.
47. Hu, C. Metal-Semiconductor Contacts. http://www-inst.eecs.berkeley.edu/~ee130/sp06/chp9.pdf) (accessed 31 March).
48. Zhou, W.; Zou, X.; Najmaei, S.; Liu, Z.; Shi, Y.; Kong, J.; Lou, J.; Ajayan, P. M.; Yakobson, B. I.; Idrobo, J.-C., Intrinsic structural defects in monolayer molybdenum disulfide. *Nano letters* 2013, 13, 2615-2622.
49. Vasilopoulou, M.; Papadimitropoulos, G.; Palilis, L. C.; Georgiadou, D. G.; Argitis, P.; Kennou, S.; Kostis, I.; Vourdas, N.; Stathopoulos, N. A.; Davazoglou, D., High performance organic light emitting diodes using substoichiometric tungsten oxide as efficient hole injection layer. *Organic Electronics* 2012, 13, 796-806.
50. Huang, D.; Wan, S.; Wang, L.; Xue, Q., One-step electrodeposition of amorphous carbon films containing WO3 with high conductivity and good wettability. *Surface and Interface Analysis* 2011, 43, 1064-1068.
51. Tamang, R.; Varghese, B.; Mhaisalkar, S. G.; Tok, E. S.; Sow, C. H., Probing the photoresponse of individual Nb2O5 nanowires with global and localized laser beam irradiation. *Nanotechnology* 2011, 22, 115202.
52. Mukherjee, B.; Hu, Z.; Zheng, M.; Cai, Y.; Feng, Y. P.; Tok, E. S.; Sow, C. H., Stepped-surfaced GeSe 2 nanobelts with high-gain photoconductivity. *Journal of Materials Chemistry* 2012, 22, 24882-24888.